

Correlation between marine aerosol optical properties and wind fields over remote oceans with use of spaceborne lidar observations

Kangwen Sun¹, Guangyao Dai¹, Songhua Wu^{1,2,3}, Oliver Reitebuch⁴, Holger Baars⁵, Jiqiao Liu⁶, Suping Zhang⁷

5 ¹College of Marine Technology, Faculty of Information Science and Engineering, Ocean University of China, 266100 Qingdao, China

²Laoshan Laboratory, 266237 Qingdao, China

³Institute for Advanced Ocean Study, Ocean University of China, 266100 Qingdao, China

10 ⁴Institut für Physik der Atmosphäre, Deutsches Zentrum für Luft- und Raumfahrt e.V. (DLR), 82234 Oberpfaffenhofen, Germany

⁵Leibniz Institute for Tropospheric Research (TROPOS), 04318 Leipzig, Germany

⁶Laboratory of Space Laser Engineering, Shanghai Institute of Optics and Fine Mechanics, Chinese Academy of Sciences, 201800 Shanghai, China

15 ⁷Physical Oceanography Laboratory, Ocean University of China, 266100 Qingdao, China

Correspondence to: Guangyao Dai (daiguangyao@ouc.edu.cn)

Abstract. Marine aerosol is mainly produced by wind, which is also a vital element impacting the transport, evolution and dissipation of marine aerosol. The understanding of the accurate relationships between marine aerosol optical properties and wind speed will improve the global aerosol transport models, the satellite-retrieved AODs, the atmospheric correction of ocean color and the study of biogeochemical cycles. Aeolus, the worldwide first ever wind detection lidar satellite, had the ability to measure wind information and particulate optical properties simultaneously, which provide the opportunity to explore the absolutely synchronous relationships between marine aerosol optical properties and wind speeds. Furthermore, thanks to the Aeolus measurement of vertical profiles, the relationships can be discussed in different vertical layers. In this paperBy utilizing Level 2A products (particle optical properties and numerical weather prediction data) and Level 2C products (numerical weather prediction wind vector assimilated with observed wind component) provided by the Atmospheric Laser Doppler Instrument (ALADIN) onboard the Aeolus mission, and Level 2 vertical feature mask (VFM) products provided by Cloud-Aerosol Lidar with Orthogonal Polarization (CALIOP) onboard Cloud Aerosol Lidar and Infrared Pathfinder Satellite Observation (CALIPSO) mission, utilizing Aeolus data, three remote ocean areas are selected and the optical properties at 355 nm of marine aerosol are derived. The combined analysis of marine aerosol optical properties at 355 nm and instantaneous co-located wind speeds above the remote ocean areas are conducted. Eventually theirthe relationships between the optical properties at 355 nm of marine aerosol and the corresponding instantaneous co-located wind speeds of three remote ocean areas are explored and discussed at two separate vertical atmospheric layers (0-1 km and 1-2 km, correspond to the heights within and above marine atmospheric boundary layer (MABL)), revealing the marine aerosol related atmospheric background states. Pure marine aerosol optical properties at 355 nm are obtained after quality control, cloud screening and backscatter

35 ~~coefficient correction from the ALADIN observations. The spatial distributions of marine aerosol optical properties and wind speed above the study areas are presented and analysed, respectively, at two vertical layers. The statistical results of the marine aerosol optical properties along with the wind speed grids at two vertical layers. The marine aerosol extinction/backscatter coefficients and the background wind speeds show positive relationships and they were fitted by power law functions, of which the corresponding R^2 are all higher than 0.9 together with the corresponding regression curves fitted by power law functions~~
40 ~~are acquired and analysed, for each remote ocean area. Both the MABL and the higher layer above the MABL will receive the marine aerosol produced and transported by the wind from the air-sea interface. The marine aerosol load at the lower layer (MABL) is stronger than at the higher layer. The marine aerosol enhancements caused by the background wind are more intensive at the MABL. The gradient change points of marine aerosol extinction/backscatter coefficients appear during the growth of them with wind speed, above which the growth rate becomes lower. It might illustrate that the enhancement of~~
45 ~~marine aerosol driven by wind includes two phases, among which one is rapid growth phase with high dependency of wind, and another is slower growth phase after the gradient change points. The optical properties present increasing trends with wind speed in all cases, implying that the atmosphere of the two vertical layers will both receive the marine aerosol input produced and transported by the wind and the turbulence. The marine aerosol enhancement caused by the wind speed at the lower layer is more intensive than at the higher layer. As derived data from ALADIN/Aeolus, the averaged marine aerosol optical depth~~
50 ~~along ($\overline{AOD_{mar}}$) with wind speed is acquired and utilized to verify the results by the comparison with CALIPSO retrieved results reported in previous work, and besides, the averaged marine aerosol lidar ratio ($\overline{LR_{mar}}$) at 355 nm along with wind speed is~~
~~acquired and discussed along the wind speed range for the relationship between marine aerosol particle size and wind speed. The marine aerosol optical properties distributions, wind speed bins, and the marine aerosol variation tendencies along wind speed above the individual study areas are not totally similar, implying that the development and evolution of the~~
55 ~~marine aerosol above the ocean might not only be dominated by the drive of the wind, but also be impacted by other meteorological and environmental factors, e.g., atmospheric stability, sea and air temperature, or relative humidity. Combined analysis on the aerosol optical properties and wind with additional atmospheric parameters above the ocean might be capable to provide more detailed information of marine aerosol production, entrainment, transport and removal.~~

1 Introduction

60 ~~The global ocean is the largest source of natural aerosol.~~ According to the Intergovernmental Panel on Climate Change (IPCC) Fifth Assessment Report, the total emission of marine aerosol (including marine primary organic aerosol) produced from ocean is 1400 to 6800 Tg·yr⁻¹, which is considered the largest natural aerosol input to the atmosphere globally (Boucher et al., 2013). Accurate estimation of marine aerosol production, evolution and dissipation, and the knowledge of marine aerosol spatial and temporal distribution are signifiate-significant for studying the global energy budget, aerosol-cloud interactions
65 and visibility changes (Latham and Smith, 1990; Murphy et al., 1998; O'Dowd et al., 1999; Haywood et al., 1999; de Leeuw

et al., 2000; Kaufman et al., 2002; Smirnov et al., 2012). Radiative forcing caused by marine aerosol is an important component of the global energy budget. It was reported that the average marine aerosol optical depth (AOD_{mar}) is approximately 0.15 while the volume concentration of cloud condensation nuclei from marine aerosol is around 60 cm^{-3} (Kaufman et al., 2002; Lewis and Schwartz, 2004). Therefore, marine aerosol has the direct impact and the indirect impact on radiative forcing, which are scattering and absorbing solar radiation, and converting cloud microphysical properties, respectively (Murphy et al., 1998; Pierce and Adams, 2006). The knowledge of the impact of the magnitude and changes of marine aerosol emissions on the shifts in climate and marine ecosystem processes is limited (IPCC, 2021).

Marine aerosols mainly include primary sea spray particles and secondary aerosols produced by the oxidation of emitted precursors. Sea spray particles, composed of sea-salt and primary organic aerosols, are produced by wind induced wave breaking as well as the wind driving direct mechanical disruption of waves crests (O'Dowd and de Leeuw, 2007; IPCC, 2021). Moreover, as a dynamical meteorological factor, wind speed also has vital influence on the transport, evolution and dissipation of aerosols. Consequently, the wind speed is a crucial factor which governs the production and life cycle of marine aerosol (Lewis and Schwartz, 2004). Exploring the accurate relationships between marine aerosol optical depth-properties (~~AOD~~aerosol optical depth (AOD), extinction coefficient (α), backscatter coefficient (β), etc.) and wind speed ~~is-are~~ significant for improving global aerosol transport models (Jaegle et al., 2011; Madry et al., 2011; Fan and Toon, 2011), for enhancing satellite-retrieved AODs (Kahn et al., 2010; Kleidman et al., 2012), for atmospheric correction of ocean color (Zibordi et al., 2011) and for the study of biogeochemical cycles (Meskhidze and Nenes, 2010). Several efforts have been reported to explore the relationship between the AOD or aerosol extinction coefficient over the ocean and wind speed. Utilizing either satellite-retrieved AODs (Glantz et al., 2009; Huang et al., 2010; Lehahn et al., 2010; O'Dowd et al., 2010; Grandey et al., 2011) or surface (coast, island or ship)-based measurement AODs (Platt and Patterson, 1986; Villevalde et al., 1994; Smirnov et al., 1995; Wilson and Forgan, 2002; Smirnov et al., 2003; Shinozuka et al., 2004; Mulcahy et al., 2008; Lehahn et al., 2010; Adames et al., 2011; Sayer et al., 2012; Smirnov et al., 2012), major previous researches focused on the AOD measured by passive instruments (mainly sun-photometer). From these studies, various power-law or linear relationships revealing positive correlation between AODs over the ocean and surface wind speed were established. The passive instruments lack the abilities of distinguishing marine aerosol from other aerosols, acquiring vertical profiles of aerosols, and retrieving aerosol optical properties without sunlight (except for lunar-photometer) and under cloudy conditions (Kiliyanpilakkil and Meskhidze, 2011; Winker and Pelon, 2003). Active optical instruments for aerosol measurements, mainly like lidar, were also used in revealing the relationship between AOD/extinction coefficient of marine aerosol and wind speed. A shipborne depolarization lidar was occupied to acquire aerosol extinction coefficients over the East Sea of Korea near Busan and Pohang, associated with the measurement of an anemometer mounted on a mast, finding a positive linear relationship ($R^2=0.57$) between extinction (532 nm) at $300 \pm 50 \text{ m}$ and wind speed at 20 m (Shin et al., 2014). However, this relationship was established with data offshore thus it can not be representative for the global ocean. Cloud-Aerosol Lidar with Orthogonal Polarization (CALIOP) onboard Cloud-Aerosol Lidar and Infrared Pathfinder Satellite Observation (CALIPSO) mission is

capable of measuring the global aerosol optical properties vertical distributions and recognizing aerosol types (include “clean marine”). Kiliyanpilakkil and Meskhidze (2011) selected CALIOP-retrieved pure AOD_{mar} below 2 km over ocean by utilizing the CALIOP aerosol subtype products and combined them with the surface wind speed provided by the Advanced Microwave Scanning Radiometer (AMSR-E) on board the Aqua satellite, acquiring a relatively complex increasing regression function, which will be presented and compared in Section 4.4.2 of this paper. Besides, Prijith et al. (2014) also made use of CALIOP-retrieved AODs below 0.5 km over ocean and the surface wind speed, obtaining nearly positive correlation linear relationships. Nevertheless, the assumed marine aerosol lidar ratio (LR_{mar}) ~~lidar ratio~~ (20 sr at 532nm) is used in the AOD_{mar} retrieval process of CALIOP (Kiliyanpilakkil and Meskhidze, 2011), but the LR_{mar} ~~lidar ratio of marine aerosol~~ can vary from 5-10 sr to ~~more than~~around 30-40 sr at 532 nm (Groß et al., 2013; Groß et al., 2015; Bohlmann et al., 2018; Floutsi et al., 2023), which could generate deviations during the retrieval of AOD_{mar} . In summary, to explore the accurate relationship between the marine aerosol optical properties and the wind speed, it is essential to conduct global continuous observations and obtain the information of aerosol type identification, while vertical profiles of aerosols can provide extra spatial information for further analysis. Moreover, previous studies mostly focused on the layer AOD_{mar} and ocean surface wind speed, exploring the probable production of marine aerosol driven by surface wind. The relationship between the vertical marine aerosol optical properties and the corresponding spatiotemporally synchronous wind speed is still to be investigated, which represents the marine-atmospheric background state and may reveal the transport and evolution of the marine aerosol vertically.

Atmospheric Laser Doppler Instrument (ALADIN) ~~is-was~~ a first ever spaceborne direct detection wind lidar, as the single payload installed on the Aeolus mission from the European Space Agency (ESA), which was launched into space in August 2018 (Stoffelen et al., 2005; Reitebuch et al., 2012; Kanitz et al., 2019). As a direct detection high-spectral-resolution lidar, ALADIN has the capability in providing the global aerosol optical properties (e.g., α and β) profiles at 355 nm (Level 2A product), the horizontal-line-of-sight (HLOS) wind speed profiles (Level 2B product), and the wind vector profile from the European Centre for Medium-Range Weather Forecasts (ECMWF) model along the Aeolus track (Level 2C product) (Rennie et al., 2020). It should be emphasized that the aerosol and wind product are retrieved from the backscattered signal of the same laser light pulse emitted from ALADIN to the atmosphere, hence the geolocation and time information of these products is completely consistent for every profile. The detection altitude range of these products is from the earth surface to around 20 km and the vertical resolutions varies from 0.25 km to 2 km (from bottom to top). Though regarded as a by-product, the particle optical property products are still demonstrated to provide valuable information about particles, especially on the detection and characterization of aerosol and cloud layers and on the lidar ratios (LRs) (Baars et al., 2021; Flament et al., 2021; Abril-Gago et al., 2022). It should be emphasized that the lowest altitude bins of Aeolus Level 2A and Level 2B products could be contaminated by reflections from the land or ocean surface, and are thus not representative for the atmospheric wind speed and the aerosol optical properties (Wu et al., 2022). Dai et al. (2022) conducted the first attempt on the combined application of the aerosol products (Level 2A products) and the wind vector products (Level 2C products) of ALADIN, observing an

enormous dust transport event occurred in June 2020 from the Sahara to the Americas, describing the transport quantitatively by calculating dust advection.

As mentioned above, Aeolus can provide global high spatial and temporal resolution aerosol optical properties profiles and wind speed profiles despite the lack of the lowest bins close to the ground. Additionally, CALIOP can provide global aerosol types information. Hence, the combination of Aeolus-CALIOP products is capable of analysing the relationship between the marine aerosol optical properties (e.g., α , β , AOD , LR) at 355 nm and wind speed globally and vertically. In this paper, by utilizing Aeolus Level 2A, Level 2C products and CALIOP aerosol subtype products, we firstly 1) select ocean areas far from land and examine the domination of marine aerosol over these areas with the CALIOP aerosol classification products, and then 2) try to acquire the pure marine aerosol optical properties (α , β , AOD , LR) at 355 nm and the corresponding wind speeds from Aeolus products, and to analyse the spatial distributions of those atmospheric state parameters at two separate vertical layers (ocean surface to 1 km, 1 km to 2 km, corresponding to the layers within and above the marine atmospheric boundary layer (MABL), respectively), and finally 3) explore the relationship between the marine aerosol optical properties and the wind speeds vertically above ocean. Generally, the highlights of this work mainly include 1) ~~first ever deriving pure marine aerosol optical properties from Aeolus products~~ 2) acquiring the spatiotemporally synchronous relationship ~~with between~~ the aerosol optical properties (α , β , LR) and the instantaneous wind speeds, which could indicate the background atmosphere states within and above the MABL over remote ocean, 3) ~~conducting analysis at two separate height layers above ocean surface to explore the vertical differences in aspect of the wind-drive marine aerosol evolution, and~~ 4) ~~selecting low latitude regions and middle latitude regions in the Southern Hemisphere and Northern Hemisphere as study areas respectively.~~

The paper is organized as follows: section 2 introduces the spaceborne lidars and their specific products used in this study; section 3 provides the methodology of study areas selection, data pre-processing and data analyses for relationship exploration between marine aerosol optical properties and wind speed; section 4 presents the procedure of study areas selection, then analyses and discusses the marine aerosol optical properties, the wind speed, and their relationship above three selected areas.

2 Spaceborne lidars and products

2.1 ALADIN/Aeolus

Since its launch in August 2018, ALADIN, has been globally observing the profiles of the component of the wind vector along the laser's line of sight (LOS), and the profiles of aerosol optical properties, for more than four years. Aeolus flies at a mean altitude of about 320 km in a sun-synchronous orbit with the local equatorial crossing time of about 06:00 and 18:00, a daily quasi-global coverage (about 16 orbits per day) with an orbit repeat cycle of 1 week (111 orbits) (Reitebuch, 2012). Designed as a high-spectral-resolution lidar with a laser wavelength of 354.8 nm, ALADIN has the ability to acquire wind profiles and particle optical properties simultaneously with its two separate optical frequency discrimination channels named as Rayleigh

channel and Mie channel. The detailed descriptions of the instrument design and the measurement concept are introduced in, e.g., Ansmann et al. (2007), Dabas et al. (2008), Flamant et al. (2008), Reitebuch (2012), Lux et al. (2020) and Flament et al. (2021).

165 Processed in different phases, Aeolus data products are classified at several levels: Level 0 (instrument housekeeping data),
Level 1B (engineering-corrected HLOS winds), Level 2A (aerosol and cloud layer optical properties), Level 2B
(meteorologically representative HLOS winds) and Level 2C (Aeolus-assisted wind vectors) (Flamant et al., 2008; Tan et
al., 2008; Rennie et al., 2020). It should be emphasized that Level 2C wind vectors are the outputs from the assimilation of the
Aeolus Level 2B products in the ECMWF numerical weather prediction (NWP) operational model after 9 January 2020
170 (Rennie et al., 2021). In addition, the products of Aeolus are available into different Baselines which correspond to different
processor versions used to derive the products. The products were firstly released as Baseline 07 at the beginning and updated
to Baseline 14 until this study is conducted. As mentioned above, we use Level 2A and Level 2C products of Aeolus for the
study of the relationship between marine aerosol optical properties and wind speeds. As the because Level 2C products can
provide both components of the wind vector that we use Level 2C instead of Level 2B products of Aeolus. The time coverage
175 of Aeolus products used in this study is from 20 April 2020 to 4 July 2022. Thus, in the aspect of the utilized Level 2A products,
the data processors are Baseline 11 (20 April 2020 to 26 May 2021), Baseline 12 (26 May 2021 to 6 December 2021), Baseline
13 (6 December 2021 to 29 March 2022) and Baseline 14 (29 March 2022 to 4 July 2022), while as for the Level 2C products,
the data processors are Baseline 09 (20 April 2020 to 9 July 2020), Baseline 10 (9 July 2020 to 8 October 2020), Baseline 11
(8 October 2020 to 26 May 2021), Baseline 12 (26 May 2021 to 6 December 2021), Baseline 13 (6 December 2021 to 29
180 March 2022) and Baseline 14 (29 March 2022 to 4 July 2022), respectively (<https://aeolus-ds.eo.esa.int/oads/access/>, last
access: 16 February 2023). The Level 2C NWP wind vector products from ECMWF used in this study are obtained after
assimilation of the Level 2B observed HLOS wind products.

2.2 CALIOP/CALIPSO

CALIOP, one of the payloads installed on CALIPSO, has been measuring global vertical aerosol and cloud optical properties
185 profiles for more than 16 years since 2006. It can provide α at 532 nm and 1064 nm, β at 532 nm and 1064 nm,
depolarization ratio at 532 nm, vertical feature mask (VFM) products and so on (Winker et al., 2009). The VFM products
comprise the vertical information along every profile on the identification of clouds and aerosols, and further, on the subtype
classification of clouds and aerosols. For cloud and aerosols identification, the cloud-aerosol discrimination (CAD) algorithm
is applied based on layer-integrated volume depolarization ratio, layer-integrated total attenuated color ratio~~layer averages of~~
190 ~~attenuated backscatter at 532 nm, layer-mean attenuated backscatter at 532 nm, latitude~~~~attenuated total color ratio~~ and ~~the mid-~~
~~layer~~-altitude (Liu et al., 2019). The aerosol sub-types are distinguished as “marine”, “dusty marine”, “dust”, “polluted dust”,
“continental”, “polluted continental”, “elevated smoke” and “others” via the joint analysis of particulate depolarization ratio,
integrated attenuated backscatter coefficient at 532 nm, layer top altitude, layer base altitude and surface type (Kim et al.,
2018). In this study, CALIOP Level (L2) VFM products are applied to confirm the domination of the marine aerosol over the

195 selected ocean areas. Different versions of the CALIOP L2 VFM product are used, respectively, the versions are 4.10 (20 April 2020 to 1 July 2020), 4.20 (1 July 2020 to 19 January 2022) and 3.41 (19 January 2022 to 4 July 2022).

3 Methodology

200 In general, the data processing and analysis procedure of this study can be concluded briefly as three parts including selection of the study areas, data pre-processing and data analyses, respectively, ~~as shown in Fig. 1.~~ The flowchart of the study methodology is shown as Fig. 2.

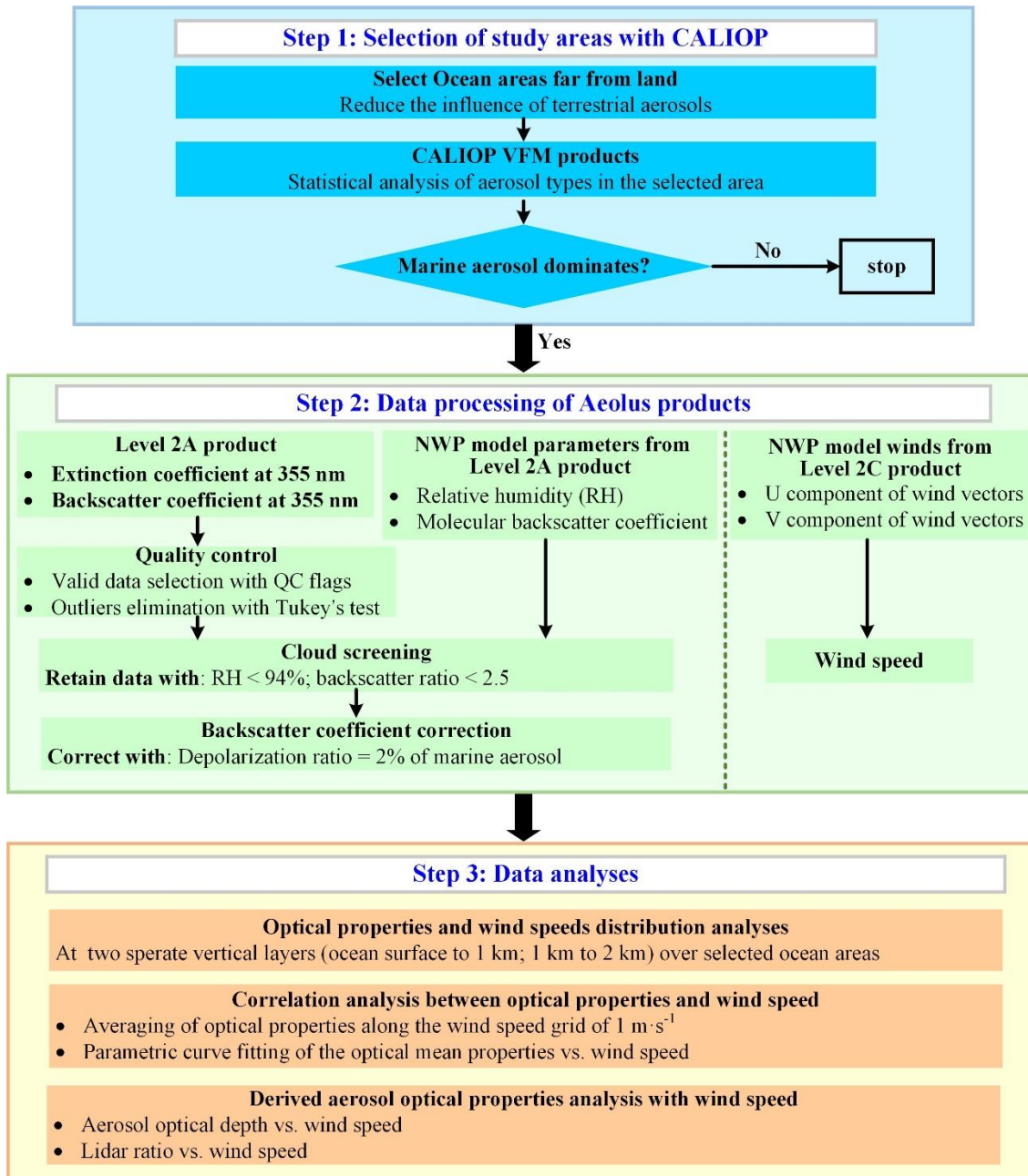
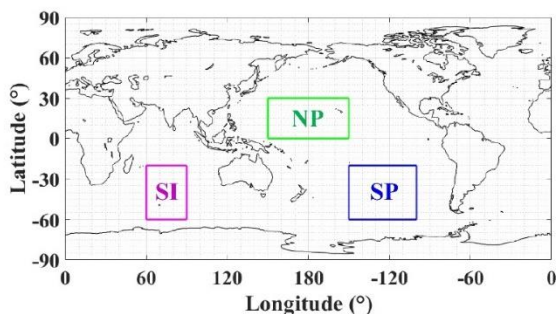


Figure 1: Flowchart of the study methodology

205 Firstly, this work mainly focuses on the marine aerosol, hence the ocean areas for the study are supposed to be far away from land to reduce the influence of terrestrial aerosols-, e.g. anthropogenic, dust, biomass burning. In this work, we selected three ocean areas located in the North Pacific ocean, South Pacific ocean, South Indian ocean, with the latitude and longitude range of 0° to 30° N and 150° E to 180° to 150° W, 20° S to 60° S and 100° W to 150° W, 20° S to 60° S and 60° E to 90° E, respectively, as shown in Fig. 1. Hence, we call these three remote ocean areas “the NP area”, “the SP area” and “the SI area” in this paper, respectively.



210

Figure 1: The selected study ocean areas.

-The aerosol classification information from CALIOP VFM products are utilized to statistically analyse the aerosol types of the selected areas. It is found that the marine aerosols are mostly distributed at the altitude range of 0 km to 2 km during the VFM processing. Therefore, the statistical analysis of aerosol types is conducted at the same altitude range. It is considered that the marine aerosol dominates in the selected area if the percentage of aerosol subtype “marine” is larger than 75% meanwhile the percentage sum of “marine” and “dusty marine” is above 90%, then the study can be continued for this area.

α at 355 nm and β at 355 nm retrieved by the standard correction algorithm (SCA) from Aeolus Level 2A product are used in this study, as the SCA processing is capable to produce more stable α and β -than other algorithms the Mie channel algorithm (Flament et al., 2021). Furthermore, the mid-bin product (sca_optical_properties_mid_bins) of the SCA product are chosen as a result from that the product retrieved as the mid-bin algorithm is more robust (Baars et al., 2021; Flament et al., 2021). To ensure a high data quality and hence to acquire the relationship between the optical properties and wind speed, a rigorous quality control has to be applied. In the aspect of quality control, negative α extinction coefficients and β backscatter coefficients are excluded, and then the quality flags (“bin_1_clear” and “processing_qc_flag”) provided in the Level 2A product are applied to filter out invalid data (Traapon et al., 2022). Additionally, the outliers are eliminated by the method of Tukey’s test. By using the lower quartiles Q_L (25% positions of the data) and upper quartiles Q_U (75% positions of the data), this method classifies the data below $Q_L - 3 \cdot (Q_U - Q_L)$ or above $Q_U + 3 \cdot (Q_U - Q_L)$ as outliers (Hoaglin et al., 1986). As the Aeolus products do not distinguish the aerosol layers and cloud layers, the marine aerosol optical properties may be contaminated by the cloud layers. Aeolus measured particulate β , combined with The relative humidity (RH) and molecular β backscatter coefficient of each data bin from the ECMWF NWP model of ECMWF are provided in the Level 2A product

230 ~~and~~ are utilized to screen the cloud layers. It is considered that a cloud is quite likely to exist if the backscatter ratio (BR) (total backscatter coefficient/molecular backscatter coefficient) at 355 nm is larger than 2.5 ~~the RH is larger than 94%~~ or the RH is larger than 94% ~~the backscatter ratio (BR) (total backscatter coefficient/molecular backscatter coefficient) at 355 nm is larger than 2.5~~ (Flamant et al., 2020). Therefore, in this study, when the BR is larger than 2.5 ~~the RH is higher than 94%~~ or the RH is higher than 94% ~~the BR is larger than 2.5~~, the corresponding data bin is regarded as cloud contaminated and is eliminated.

235 With this cloud screening approach, in this study, 9%, 35%, 40% data in the altitude range of 0-2 km was eliminated for the NP area, the SP area and the SI area, respectively. Due to the instrument design of ALADIN, it can only detect the co-polar backscatter light, leading to the lack of the depolarized portion of the β ~~backscatter coefficient~~ (Flamant et al., 2020). According to Groß et al. (2015), the depolarization ratio at 355 nm of marine aerosol ($\delta_{mar,355nm}$) is approximately 0.02 when the RH is larger than 50%. Nevertheless, dried marine aerosol layers can significantly depolarize and the depolarization ratio

240 will vary from 0.02 to around 0.1, so the typical $\delta_{mar,355nm}$ of humid marine aerosol (RH>50%) is not suitable for dried aerosol (Haarig et al. 2017; Bohlmann et al. 2018). Consequently, to correct the marine aerosol backscatter coefficient with the typical $\delta_{mar,355nm}$ of humid marine aerosol, the data with RH>50% is retained (around 95% data is retained), and thus with the typical $\delta_{mar,355nm}$ the total marine aerosol backscatter coefficient β_{mar} can be calculated by the following Eq. (1):

$$\beta_{mar} = (1 + \delta_{mar,355nm}) \cdot \beta_{mar,Aeolus-co}, \quad (1)$$

245 where $\beta_{mar,Aeolus-co}$ is the original marine aerosol backscatter coefficient measured by ALADIN. It should be illustrated that all the aerosol β s from Aeolus identified as $\beta_{mar,Aeolus-co}$ s and then utilized to calculate β_{mar} s by formula (1) is under the ideal assumption that marine aerosol is the only aerosol type in the study areas. Though the study areas are all located in the remote ocean far away from land and are evaluated as “marine aerosol dominate” by CALIOP, there are a few terrestrial aerosols like dust, polluted dust, polluted continental and smoke, with the total proportion of no more than 10% (see Section 4.1 for the

250 detail). For the part of terrestrial aerosols, the depolarization ratios at 355 nm of them are 0.22-0.24 for dust, 0.16 for polluted dust, 0.01 for polluted continental and 0.03 for smoke, among which the dust’s and the polluted dust’s are much larger than $\delta_{mar,355nm}$ (Floutsis et al., 2023). Consequently, regarding all the aerosols as marine aerosol and correcting β_{mar} by formula (1) leads to the obvious underestimation of the β for dust and polluted dust. Nevertheless, in view of the small proportions of dust (no more than 3.15%) and polluted dust (no more than 0.79%) above the study areas and thanks to the statistical analyses

255 of data for a long term, the assumption that regarding all the aerosols as marine aerosol is considered not to critically impact the β_{mar} - wind speed relationship, while it should be noticed that the actual β is a little bit larger than the β_{mar} .

As for the wind vector data, Aeolus Level 2C product provides the u component (zonal components of wind vector) and v component (meridional components of wind vector) from the ECMWF model after assimilation of Level 2B observational wind product, at the same data bins of the Level 2A optical properties product. Hence the wind speed ws can be calculated

260 with these two components by the following Eq. (2):

$$ws = \sqrt{u^2 + v^2} . \quad (2)$$

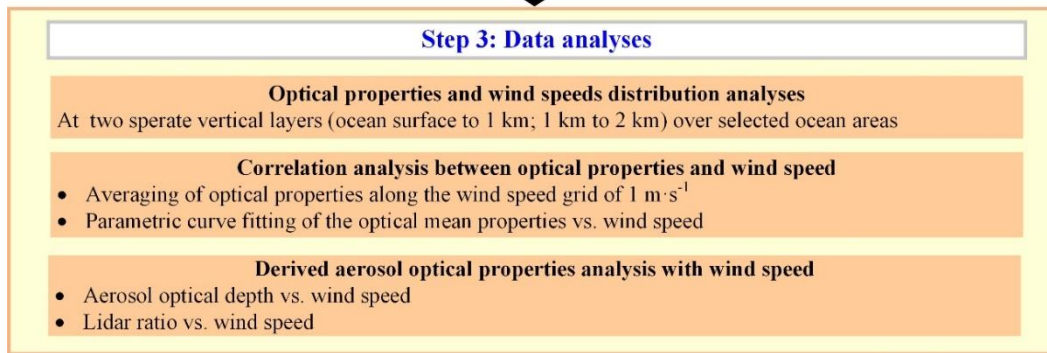
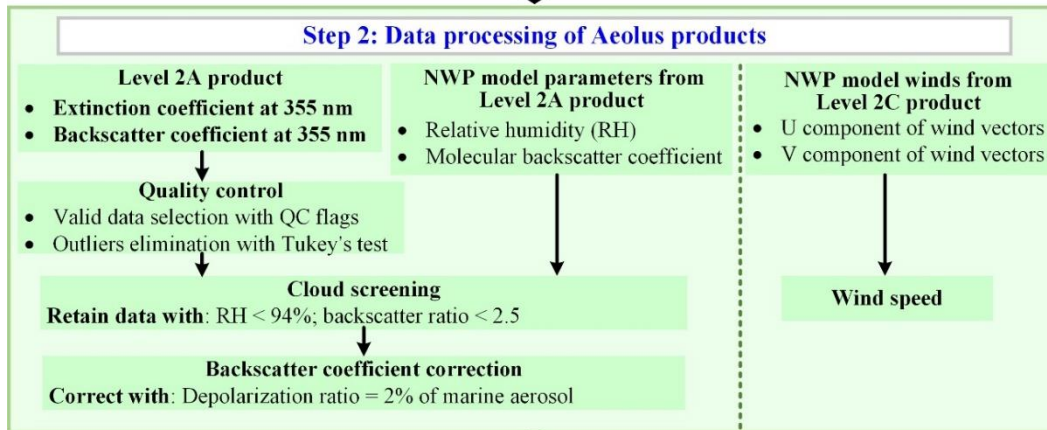
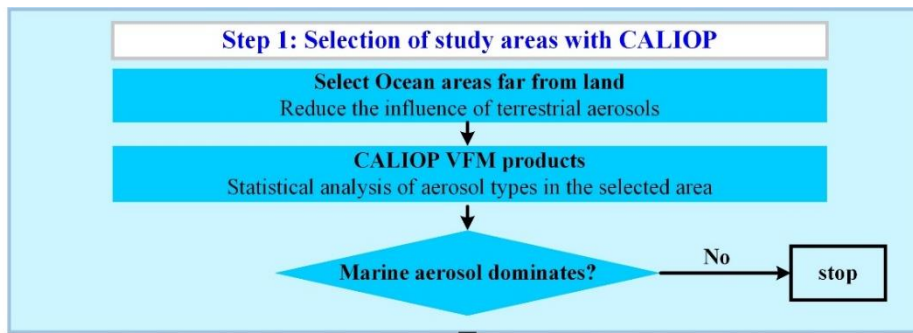
With the re-processed marine aerosol optical properties extinction coefficient α_{mar} and β_{mar} , and the corresponding ws , it is possible to explore the relationship between these parameters. At the beginning of data analyses, α_{mar} , β_{mar} and ws within the altitude range of 0 km to 2 km are selected, where the marine aerosol dominates according to the analysis of CALIOP VFM. Further, the whole study height range is divided into two individual layers. Referring the results of Luo et al. (2014), Luo et al. (2016) and Alexander et al. (2019), Considering that the MABL height of the remote ocean is summarized as around 1 km. Moreover, calculated with ECMWF provided boundary layer heights at the three study areas for the time period of 20 April 2020 to 26 May 2021 (Luo et al., 2014; Luo et al., 2016; Alexander et al., 2019), the mean values and the standard deviations are 787.47 ± 231.77 m at the NP area, 939.39 ± 360.20 m at the SP area and 1005.29 ± 366.60 m at the SI area.

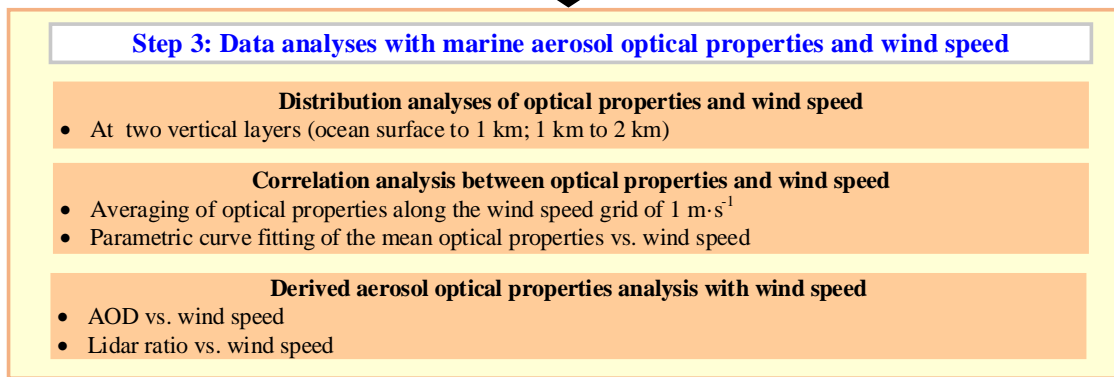
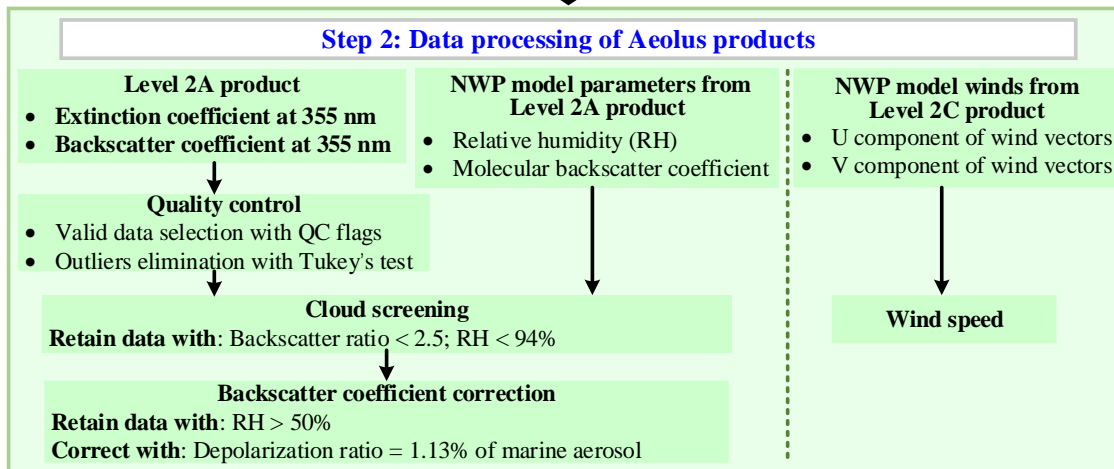
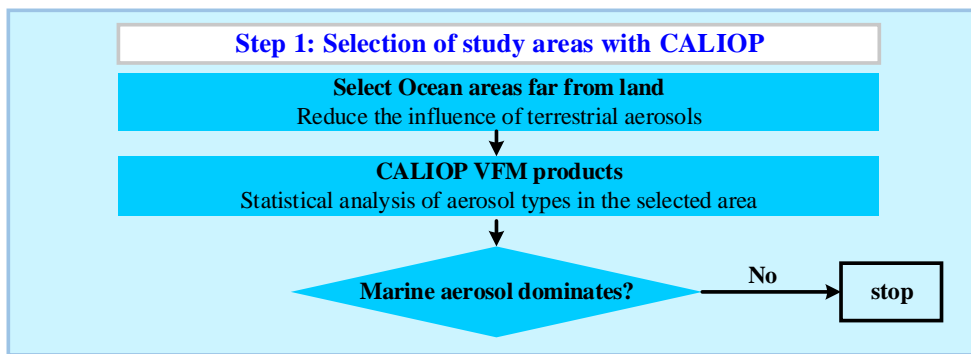
Hence, the boundary height of the two vertical layers is set as 1 km, approximately corresponding to the mean MABL height of remote ocean. Though the MABL heights are variable and thus set as 1 km will lead to the potential inaccuracies, restricted by the relatively low height resolution of Aeolus (0.25 km below 0.5 km, 0.5 km in the range of 0.5 km to 2 km), utilizing more precise height boundaries won't make more sense. It is considered that the statistical results of the 0-1 km layers and the 1-2 km layers are capable to generally represent the atmospheric conditions in this study to explore the difference between

within the MABL and above the MABL. The lower layer with the altitude range of 0 km to 1 km Among them one is called Layer_L in this paper, which corresponds to the MABL with the altitude range of 0 km to 1 km, and another the higher layer with the altitude range of 1 km to 2 km is called Layer_H, above the MABL with the altitude range of 1 km to 2 km. It should be emphasized that in Layer_L, the lowest Aeolus Level 2A products (particle optical properties) data bins with the altitude of lower than about 0.25 km, are absent to avoid the ground return signals' contamination. This leads to that the actual marine aerosol optical properties altitude range of Layer_L is around 0.25 km to 1 km. Over the selected ocean areas, the spatial distribution of the α_{mar} , β_{mar} and ws are acquired with the longitude-latitude grid of $5^\circ \times 5^\circ$ at two separate layers. Then the relationship analyses between the optical properties (α_{mar} , β_{mar}) and ws of these two layers are conducted by the average calculations of the optical properties along ws grids ($1 \text{ m} \cdot \text{s}^{-1}$) and the parametric curve fitting. For the average calculations, specifically, a grid with resolution of $1 \text{ m} \cdot \text{s}^{-1}$ from $0 \text{ m} \cdot \text{s}^{-1}$ to $30 \text{ m} \cdot \text{s}^{-1}$ is defined and the mean values and the standard deviations are calculated along the grid at both layers above the study areas, respectively. It should be emphasized primarily that before the calculation of mean of each wind speed grid, the outliers larger/less than the mean plus/minus one standard deviation are eliminated. About 70% to 80% α_{mar} and β_{mar} are retained after the elimination. The quite strict outlier removal is conducted here to reject the data unrepresentative for marine aerosol (may be contaminated by cloud thus become higher than the typical range). Hence, it can guarantee the data quality and validity of the pure marine aerosol optical properties in

the statistical analysis process. Moreover, the wind speed grid of which the data counts are less than 100 is considered unrepresentative and the statistical result of this grid is abandoned. The derived data of α_{mar} , β_{mar} , averaged AOD_{mar} **marine**

~~aerosol optical depth~~ (\odot) and ~~LR_{mar} marine aerosol lidar ratio~~ (\odot) are obtained and discussed, as well. The AOD_{mar} is acquired by integrating Aeolus retrieved α_{mar} within 2 km of every single profile. The AOD_{mar} is calculated within the height of 2 km in order to compare with the previous result of CALIOP, where the integration height is the same as that in this study. The averaged AOD_{mar} along the ws grid are obtained and then are compared with the AOD_{mar} - ws relationships from a previous study in Section 4.4.1. The LR_{mar} are derived via dividing α_{mar} by β_{mar} for each corresponding data bin. The spatial distribution of the LR_{mar} are presented in Section 4.2, meanwhile the relationship between the variations of the LR_{mar} along ws grids and the marine aerosol particle size are discussed in Section 4.4.2.





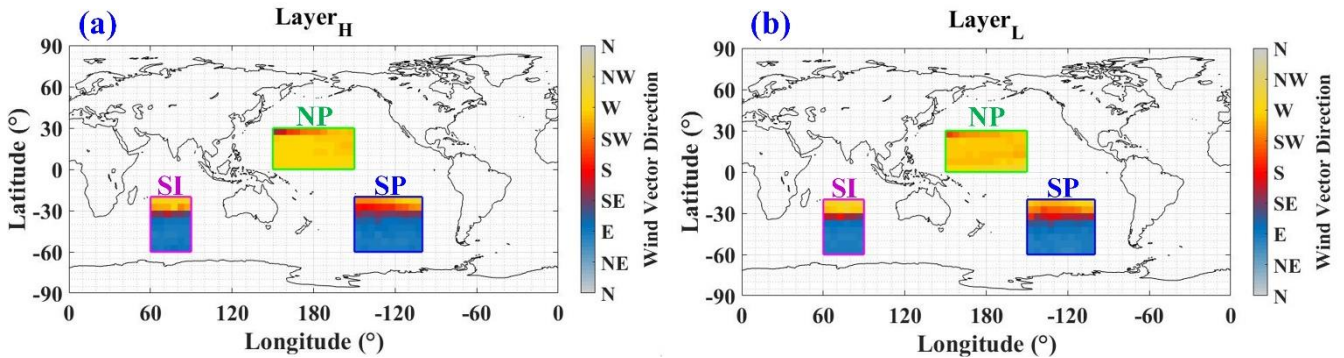
300

Figure 12: Flowchart of the study methodology.

4 Results and discussion

4.1 Study areas selection and aerosol types analysis

305 To focus this study only on marine aerosol, the study areas should be far away from continents and rarely affected by aerosol from land surfaces, e.g. anthropogenic, dust, biomass burning. The selected ocean areas are located in the North Pacific ocean, South Pacific ocean, South Indian ocean, with the latitude and longitude range of 0° to 30° N and 150° E to 150° W, 20° S to 60° S and 100° W to 150° W, 20° S to 60° S and 60° E to 90° E, respectively, as shown in Fig. 2. Hence, we call these three remote ocean areas “the NP area”, “the SP area” and “the SI area” in this paper, respectively.



310

Figure 2: The selected study areas and their wind vector direction distributions above (a) $Layer_H$ (1-2 km, above the MABL) and (b) $Layer_L$ (0-1 km, correspond to the MABL). All the three study areas are far away from the lands. The colors in the boxes indicate the wind vector directions.

Wind is the major driver for aerosol transport. Hence, firstly the $5^{\circ} \times 5^{\circ}$ grid averaged wind directions of $Layer_H$ and $Layer_L$ are calculated and presented in Fig. 2. From the distributions, it can be seen that the wind directions of $Layer_H$ and $Layer_L$ are quite similar to each other. The NP area is dominated by westward wind with a small proportion of southward wind in the northwest of this area while the eastern side of this area is far away from land. As a result, it is inferred that the terrestrial aerosol is rarely going to be transported to the NP area. In terms of the SI area and the SP area, of which the wind direction distributions are similar, from south to north, the wind directions vary from eastward to southward and then to westward. Moreover, there is no continent or the continent is far away in the upwind of the SI area and the SP area. Hence, it indicates that these two areas are rarely influenced by other aerosols from lands as well.

320

To further verify the domination of marine aerosol, as introduced in Section 3 of this paper, the CALIOP VFM aerosol classification products are applied. The proportions of eight aerosol types (marine, dusty marine, dust, polluted dust, continental, polluted continental, smoke and others) are counted at two vertical layers defined in Section 3 over the NP area, the SP area and the SI area, respectively, as shown the histograms in Fig. 3. The proportions of marine aerosol at $Layer_L$ in these three separate areas are 87%, 84% and 84% while the proportions at $Layer_H$ are 84%, 79% and 79% respectively, which

325

are all larger than 75%. Moreover, the percentage sums of marine aerosol and dusty marine aerosol are all above 90%, at both layers and over all study areas. Consequently, the selected areas NP, SP and SI can be regarded as the marine aerosol dominating areas. It should be illustrated that “dusty marine” was a new aerosol subtype raised for the first time in the version 4.10 of the CALIOP VFM product and was absent in the version 3.41, which was identified from part of version 3.41’s “polluted dust” with the criteria of “surface type” and “layer base altitude”. Using the version 3.41 of the CALIOP VFM data for the period of 19 January 2022 to 4 July 2022 led to the underestimate of “dusty marine” portion and the total marine aerosol portion. Even though under the condition of underestimate, the percentage of total marine aerosol are larger than 90%, which means the real proportion of total marine aerosol is higher, and hence the conclusion that the marine aerosol dominates in the altitude range of 0-2 km above these three areas is still valid.

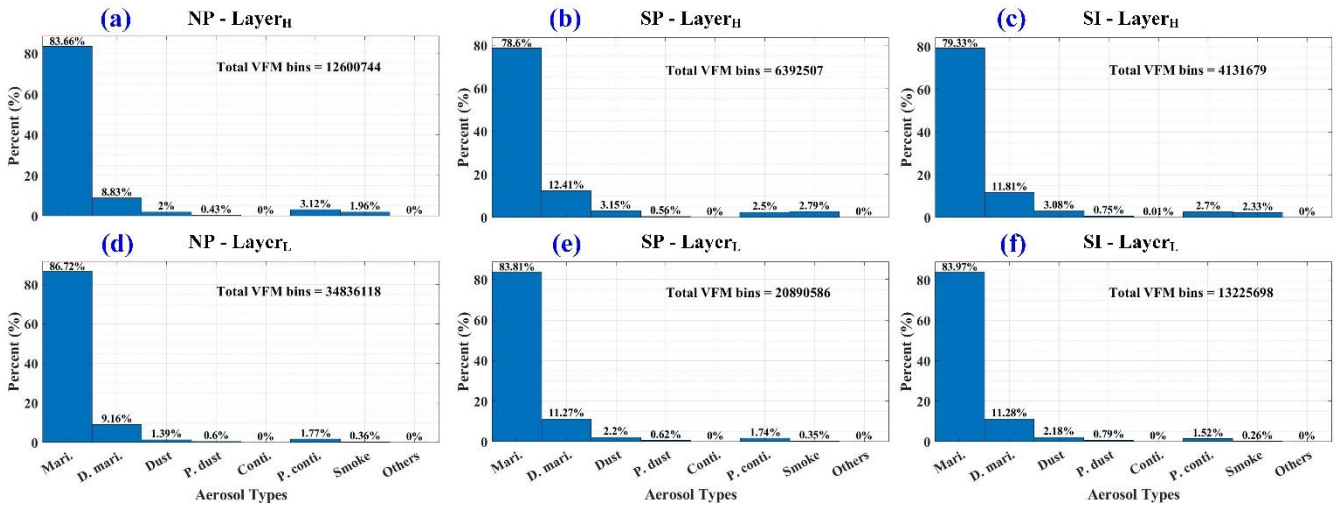


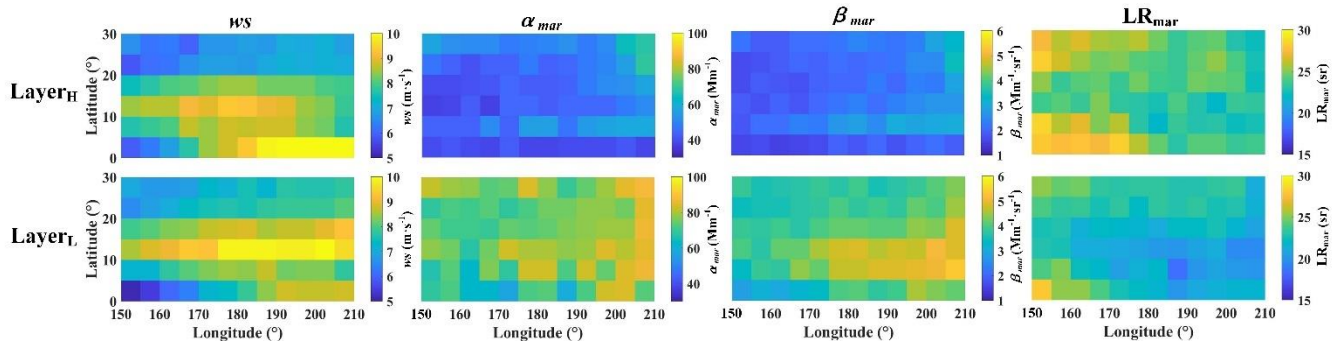
Figure 3: Aerosol types statistical analyses over (a)(d) the NP area, (b)(e) the SP area and (c)(f) the SI area at two separate layers.

In this section, the study areas in this paper are introduced. With ~~the wind direction distribution analyses and~~ the aerosol types statistical analyses, the dominations of marine aerosol are confirmed over these three areas. It should be illustrated that among the areas, the NP area is mainly located in low latitudes or tropics, while the SP area and the SI area are in mid-latitude region.

4.2 Spatial distribution of wind speed and aerosol optical properties

With Aeolus L2A products (particle optical properties) and L2C products (ECMWF model winds) from April 2020 to July 2022, calculated for every $5^\circ \times 5^\circ$ grid, the averaged ws , α_{mar} , β_{mar} and LR_{mar} spatial distributions of Layer_H and Layer_L are acquired. The averaged atmospheric parameters spatial distributions of the NP area, the SP area and the SI area are presented in Fig. 4, Fig. 5 and Fig. 6, respectively. These figures describe the atmospheric background state of optical properties and wind speed within (Layer_L) and above (Layer_H) the MABL over the study areas. Additionally, the mean values and the

standard deviations of these atmospheric parameters at Layer_H and Layer_L are calculated for each study area by averaging the spatial distributions of $5^\circ \times 5^\circ$ grid, and are presented in Fig. 7.



350 **Figure 4:** Wind speed (WS), marine aerosol extinction coefficient (α_{mar}), marine aerosol backscatter coefficient (β_{mar}), and marine aerosol lidar ratio (LR_{mar}) spatial distributions above the North Pacific (NP) area at Layer_H and Layer_L .

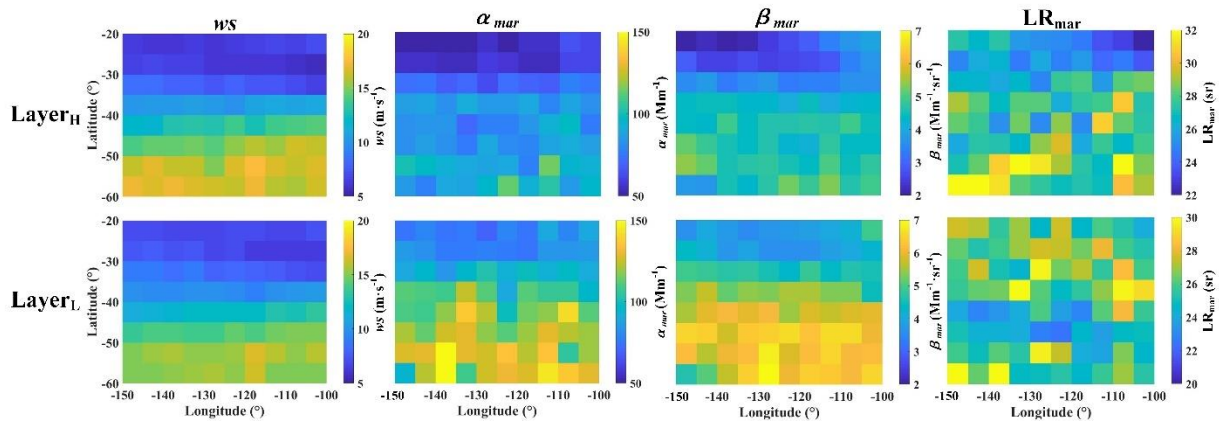


Figure 5: Wind speed (WS), marine aerosol extinction coefficient (α_{mar}), marine aerosol backscatter coefficient (β_{mar}), and marine aerosol lidar ratio (LR_{mar}) spatial distributions above the South Pacific (SP) area at Layer_H and Layer_L .

355

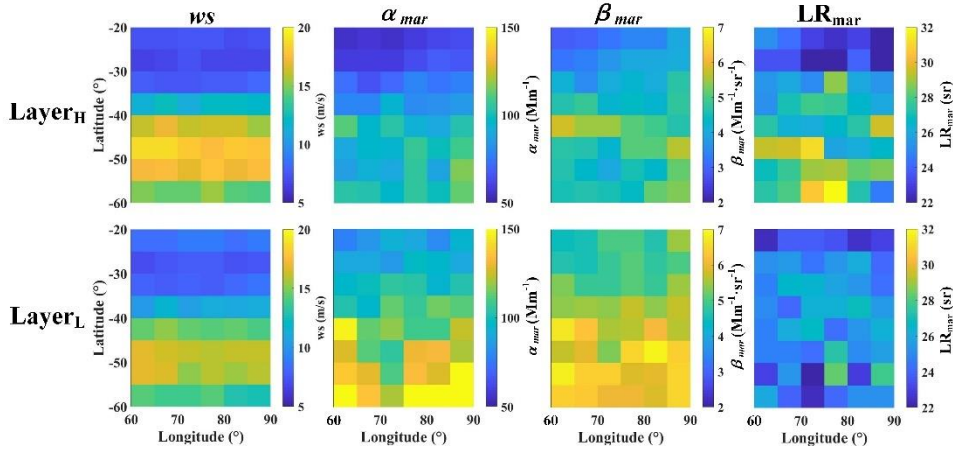
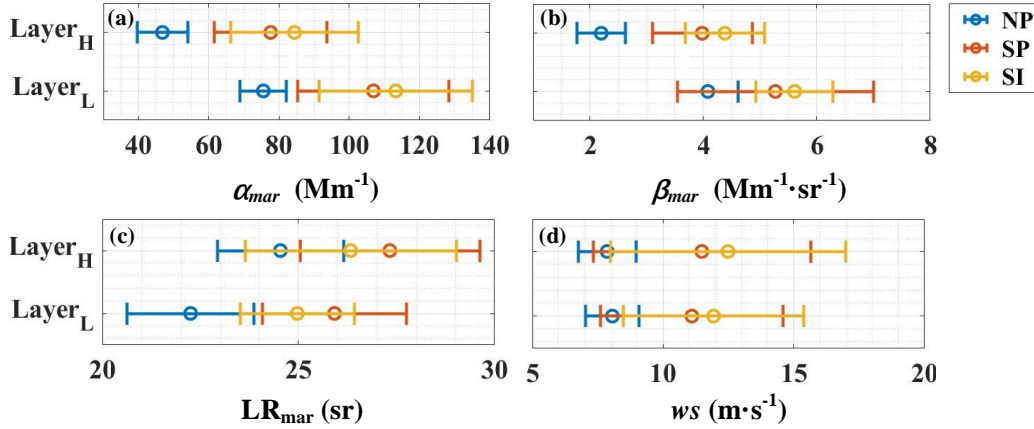


Figure 6: Wind speed (ws), marine aerosol extinction coefficient (α_{mar}), marine aerosol backscatter coefficient (β_{mar}), and lidar ratio (LR_{mar}) spatial distributions above the South Indian (SI) area at Layer_H and Layer_L.



360

Figure 7: Mean values at Layer_H and Layer_L of (a) wind speed (ws), (b) marine aerosol extinction coefficient (α_{mar}), (c) marine aerosol backscatter coefficient (β_{mar}), and (d) marine aerosol lidar ratio (LR_{mar}) and (e) wind speed (ws) above the North Pacific (NP) area (blue standard deviation bars), the South Pacific (SP) area (red standard deviation bars), and the South Indian (SI) area (yellow standard deviation bars).

365

In Fig. 7, the mean values and the deviations of the parameters represent the background atmospheric states within the MABL (Layer_L) and over the MABL (Layer_H) above each study areas. The averaged ws are $8.1 \pm 1.0 \text{ m} \cdot \text{s}^{-1}$, $11.1 \pm 3.5 \text{ m} \cdot \text{s}^{-1}$, $12.0 \pm 3.5 \text{ m} \cdot \text{s}^{-1}$ at Layer_L, while $7.9 \pm 1.1 \text{ m} \cdot \text{s}^{-1}$, $11.5 \pm 4.2 \text{ m} \cdot \text{s}^{-1}$, $12.5 \pm 4.5 \text{ m} \cdot \text{s}^{-1}$ at Layer_H, above the NP area, the SP area, and the SI area, respectively. The averaged α_{mar} are $76 \pm 7 \text{ Mm}^{-1}$, $107 \pm 22 \text{ Mm}^{-1}$, $113 \pm 22 \text{ Mm}^{-1}$ at Layer_L, while $47 \pm 7 \text{ Mm}^{-1}$, $78 \pm 16 \text{ Mm}^{-1}$, $84 \pm 18 \text{ Mm}^{-1}$ at Layer_H, above the NP area, the SP area, and the SI area, respectively. The averaged β_{mar} are $4.1 \pm 0.5 \text{ Mm}^{-1} \cdot \text{sr}^{-1}$, $5.3 \pm 1.7 \text{ Mm}^{-1} \cdot \text{sr}^{-1}$, $5.6 \pm 0.7 \text{ Mm}^{-1} \cdot \text{sr}^{-1}$ at Layer_L, while $2.2 \pm 0.4 \text{ Mm}^{-1} \cdot \text{sr}^{-1}$,

370 $4.0 \pm 0.9 \text{ Mm}^{-1} \cdot \text{sr}^{-1}$, $4.4 \pm 0.7 \text{ Mm}^{-1} \cdot \text{sr}^{-1}$ at Layer_H, above the NP area, the SP area, and the SI area, respectively. The averaged LR_{mar} are $22.3 \pm 1.6 \text{ sr}$, $25.9 \pm 1.8 \text{ sr}$, $25.0 \pm 1.5 \text{ sr}$ at Layer_L, while $24.5 \pm 1.6 \text{ sr}$, $27.3 \pm 2.3 \text{ sr}$, $26.3 \pm 2.7 \text{ sr}$ at Layer_H, above the NP area, the SP area, and the SI area, respectively. It is reported that the typical ranges of α_{mar} and β_{mar} at 532 nm over remote ocean areas are around 60 Mm^{-1} to 80 Mm^{-1} and around $1 \text{ Mm}^{-1} \cdot \text{sr}^{-1}$ to $5 \text{ Mm}^{-1} \cdot \text{sr}^{-1}$, respectively, observed and retrieved by CALIOP (Prijith et al., 2014; Kiliyanpilakkil and Meskhidze, 2011). Applying the typical α_{mar} Ångström exponent from 532 nm to 355 nm of 0.7 ± 1.3 and the typical β_{mar} Ångström exponent from 532 nm to 355 nm of 0.8 ± 0.1 (Floutsi et al., ~~2022~~2023), the converted typical ranges of α_{mar} and β_{mar} at 355 nm can be calculated, which are around 47 Mm^{-1} to 180 Mm^{-1} and around $1.3 \text{ Mm}^{-1} \cdot \text{sr}^{-1}$ to $7.2 \text{ Mm}^{-1} \cdot \text{sr}^{-1}$. Compared with the typical ranges of α_{mar} and β_{mar} at 355 nm, calculated from CALIOP retrieved and converted marine aerosol optical properties (typical α_{mar} and β_{mar}) ranges of marine aerosol optical properties and the typical conversion coefficients, it is considered that the Aeolus retrieved α_{mar} and β_{mar} are reasonable. The mean values of w_s , α_{mar} and β_{mar} above the NP area are the lowest among the three areas, both at Layer_H and Layer_L, which may be because that this area is located in low latitudes region of the Northern Hemisphere. The highest mean wind speed of the SI area corresponds to the highest α_{mar} and β_{mar} . The mean wind speeds of Layer_H are both larger than those of Layer_L in the SP area and in the SI area, while the phenomenon is on the contrary in the NP area. It is worth noting that in all the study areas, the averaged α_{mar} and β_{mar} at Layer_L are larger than those at Layer_H, illustrating that the majority of the aerosol from ocean is trapped in the MABL while a fraction of marine aerosol can be elevated above the MABL. In the aspect of mean LR_{mar}, the values at Layer_H are all higher than at Layer_L, and all the values are in a reasonable range referring to Bohlmann et al. (2018), Groß et al. (2011), Groß et al. (2015) and Floutsi et al. (~~2022~~2023). From Figure 4, Fig. 5, and to Fig. 6, overall, it can be found that presents the parameters distributions at two layers of above all three areas the NP area, the SP area and the SI area have several similar features. Primarily, the spatial variations of w_s , α_{mar} , β_{mar} are more apparent along the meridian than zonally, both at Layer_H and at Layer_L. In the aspect of Layer_L, there are separate distinct high wind speed regions or belts along latitude in the three areas, which are 5° N to 20° N region of the NP area with the wind speed bins of approximately $8 \text{ m} \cdot \text{s}^{-1}$ to more than $10 \text{ m} \cdot \text{s}^{-1}$, 40° S to 60° S region of the SP area with the wind speed bins of more than $10 \text{ m} \cdot \text{s}^{-1}$ to approximately $17 \text{ m} \cdot \text{s}^{-1}$, and 35° S to 60° S region of the ~~NP-SI~~ area with the wind speed bins of more than $10 \text{ m} \cdot \text{s}^{-1}$ to approximately $17 \text{ m} \cdot \text{s}^{-1}$ as well. Inspection of marine aerosol optical properties, α_{mar} and β_{mar} in the high wind speed regions are obviously larger than in other regions. Hence, it can be inferred that, in the MABL, the wind speed and the marine aerosol optical properties tend to be positively correlated. Referring to Layer_H, shown in the upper four panels of Fig. 4, Fig. 5 and Fig. 6, it can be found that the spatial variation trends of w_s , α_{mar} , β_{mar} in the three areas are alike with those at Layer_L. The evident high wind speed regions, where the wind speeds are up to around 8-10

$\text{m} \cdot \text{s}^{-1}$ in 5° N to 20° N of the NP area, 15-18 $\text{m} \cdot \text{s}^{-1}$ in 40° S to 60° S of the SP area and 13-19 $\text{m} \cdot \text{s}^{-1}$ in 35° S to 60° of the SI area, also exist at Layer_H while α_{mar} and β_{mar} are slightly enhanced in these regions, which indicates that the wind speed
400 may still have weak positive influence on the marine aerosol optical properties at the higher atmosphere layer above the MABL. Some spatial distribution differences of ws , α_{mar} , β_{mar} between the three areas can be discovered as well. As for the SP area and the SI area, ws , α_{mar} , β_{mar} all mainly present increasing tendencies from north to south. In term of the NP area, besides the obvious enhancements of ws , α_{mar} , β_{mar} in the high wind speed belt, the gradual enhancements of these atmospheric parameters are presented from west to east in this area.

405 At both layers of the NP area and at Layer_L of the SP area, the LR_{mar} turn out lower in the relatively high wind speed regions, which illustrates a possible negative correlation between LR_{mar} and wind speed. The relationship between these two parameters is analysed and discussed in detail in Section 4.4.2 of this paper.

To conclude, this section presents the atmospheric background state of optical properties and wind speed, and analyses the spatial distributions of ws , α_{mar} , β_{mar} jointly at Layer_H and Layer_L above the NP area, the SP area and the SI area,
410 respectively. The α_{mar} , β_{mar} retrieved from Aeolus Level 2A products are in reasonable agreement with CALIOP and the Aeolus-derived LR_{mar} are also reasonable. It is found that, both at Layer_H and at Layer_L, spatially, the wind speed and α_{mar} , β_{mar} show positive correlation though the optical properties at Layer_L are greater than those at Layer_H, indicating that both layers receive the input of the aerosol produced from ocean by the wind but the majority of the marine aerosol are trapped in the MABL while only a small fraction can be elevated into the higher layer. In addition, as the three study areas are located in
415 different regions, the spatial distributions of ws , α_{mar} , β_{mar} are different.

4.3 Relationship between marine aerosol optical properties and wind speed

~~The distributions of marine aerosol optical properties versus wind speed are discussed in this section. The data are counted with α_{mar} - ws grid bins and β_{mar} - ws grid bins at two separate layers (Layer_H and Layer_L) for the study areas. The statistical results over the NP area, the SP area and the SI area are presented in Fig. 8, Fig. 9 and Fig. 10, respectively. Though the data counts sums of each study area are different due to the difference of the areas' dimensions, the color variation of the data bins can still reveal the normalized distribution. From Fig. 8 to Fig. 10, it can be figured out that the distributions of the optical properties and the wind speeds in the NP area are the most concentrated among three areas while the data in the SI area are quite dispersed. As for the NP area, few data bins appear in the region where wind speeds are greater than $20 \text{ m} \cdot \text{s}^{-1}$, indicating that wind speed can rarely reach up to $20 \text{ m} \cdot \text{s}^{-1}$ at the altitude range of 0 km to 2 km in this low-latitude area. Nevertheless,
425 in terms of the SP area and the SI area, though the major distribution of the wind speed at Layer_H and Layer_L are in the approximate range of $0 \text{ m} \cdot \text{s}^{-1}$ to $20 \text{ m} \cdot \text{s}^{-1}$, the wind speed is reaching up to $30 \text{ m} \cdot \text{s}^{-1}$ as the bins with the wind speed of~~

430 $20 \text{ m}\cdot\text{s}^{-1}$ to $30 \text{ m}\cdot\text{s}^{-1}$ are almost all filled by blue. Between the two separate layers, these figures show no pronounced difference in the aspect of wind speed bins, whereas the optical properties at the lower layers are distinctly larger than those at the higher layers. The data distributions of α_{mar} and β_{mar} versus ws at Layer_L of three study areas ((c) and (d) panels of Fig. 8, Fig. 9 and Fig. 10) present the increasing tendency of the marine aerosol optical properties with wind speed while the tendency does not appear distinctly at Layer_H .

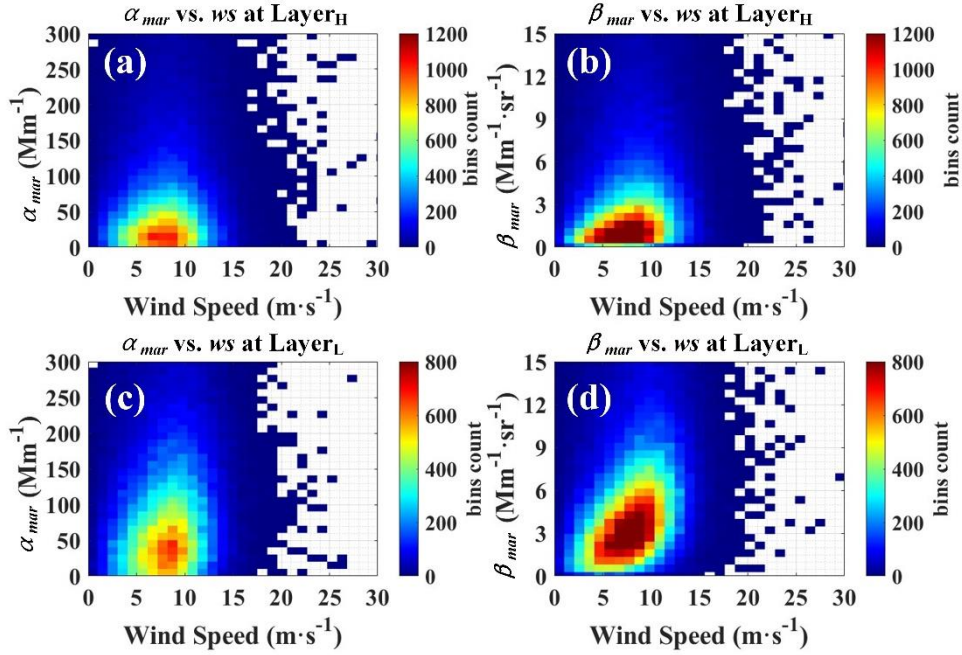
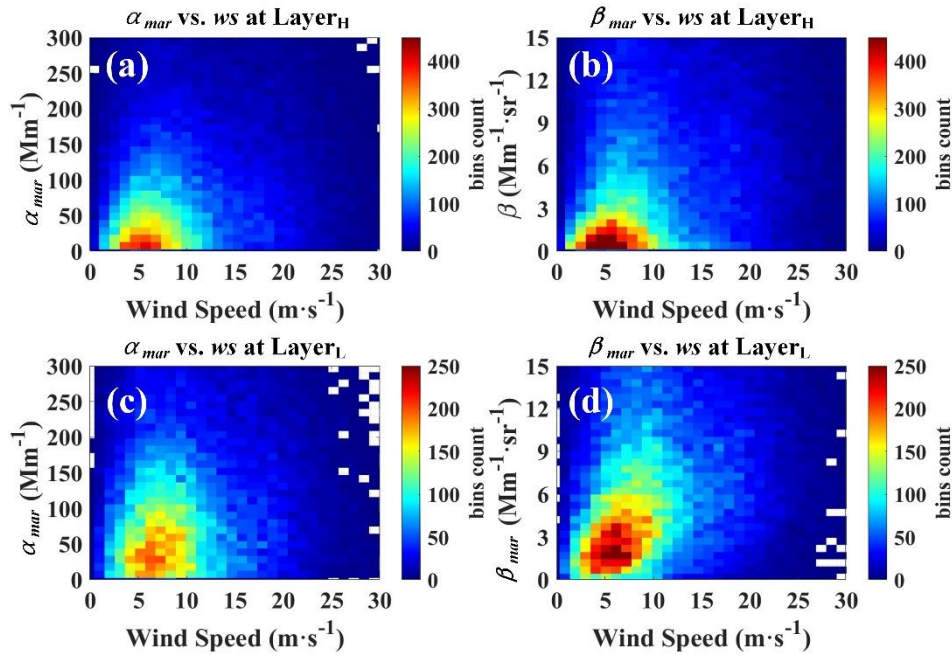


Figure 8: Data counts of α_{mar} - ws grid bins, β_{mar} - ws grid bins at separate layers above the NP area.



435 **Figure 9: Data counts of α_{mar} -ws grid bins, β_{mar} -ws grid bins at separate layers above the SP area.**

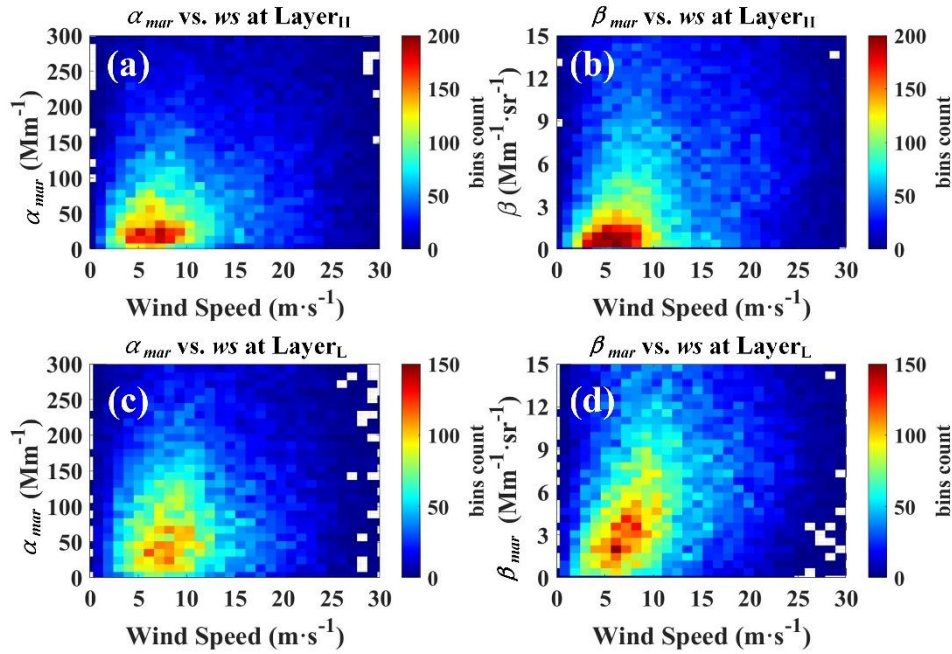


Figure 10: Data counts of α_{mar} -ws grid bins, β_{mar} -ws grid bins at separate layers above the SI area.

In order to determine the **explicit** relationship between marine aerosol optical properties and corresponding wind speed, **utilizing the method introduced in Section 3**, a grid with resolution of $1 \text{ m} \cdot \text{s}^{-1}$ ~~from $0 \text{ m} \cdot \text{s}^{-1}$ to $30 \text{ m} \cdot \text{s}^{-1}$~~ is defined and the mean values and the standard deviations are calculated along the grid at both layers above the study areas, respectively. It should be emphasized primarily that before the calculation of mean of each wind speed grid, the outliers larger/less than the mean plus/minus one standard deviation are eliminated. About 70% to 80% α_{mar} and β_{mar} are retained after the elimination. The quite strict outlier removal is conducted here to reject the data unrepresentative for marine aerosol (may be contaminated by cloud thus become higher than the typical range). Hence, it can guarantee the data quality and validity of the pure marine aerosol optical properties in the statistical analysis process. Moreover, the wind speed grid of which the data counts are less than 100 is considered unrepresentative and the statistical result of this grid is abandoned. The mean values and standard deviations (after the outlier removal) of α_{mar} and β_{mar} along with wind speed grid at two layers above the NP area, the SP area and the SI area are shown in **the panel (a) and (b) of Fig. 448, Fig. 429, and Fig. 4310**, respectively. The regression curves of the optical properties are presented in those figures as well. A **p**Power law function is utilized for the curve fitting to describe the trend of marine aerosol optical properties with wind speed. Besides, the data counts in every wind speed grid are shown as the histograms in **the panel (a) and (b) of Fig. 448, Fig. 429, and Fig. 4310**. **In order to illustrate the variation tendencies α_{mar} and β_{mar} , the gradients of α_{mar} and β_{mar} with wind speed are also provided in the panel (c) and (d) of Fig. 8, Fig. 9, and Fig. 10.** Table 1 summarizes the regression functions together with the corresponding R^2 , and the proportions of different wind speed bins together with the count sums, grouped by areas, layers and optical properties.

From the statistical results with wind speed grids and wind speed **bins** ranges, it can be found that most of the wind speeds are below $15 \text{ m} \cdot \text{s}^{-1}$ above the NP area, both at Layer_H and Layer_L, meanwhile the proportion of low wind speed ($0 < ws \leq 8$) is slightly higher at Layer_H than at Layer_L. As for the SP area and the SI area, the high wind speed ($ws > 15$) accounts for around one fifth and a quarter respectively, and the low wind speed proportion over the SP area is higher than that over the SI area. The wind speed distribution is more concentrated at Layer_L than at Layer_H above these two areas, in view of the lower proportion of low/high wind speed and the higher proportion of middle wind speed ($8 < ws \leq 15$) at Layer_L.

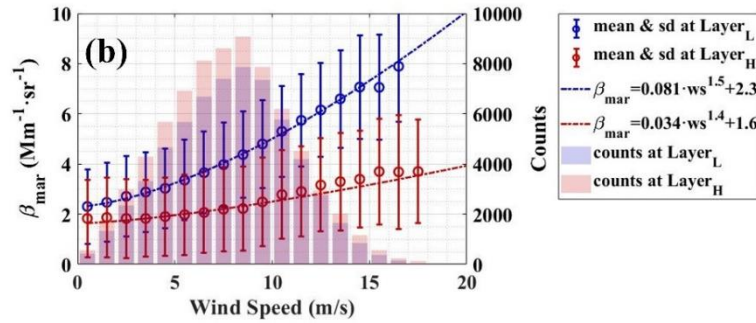
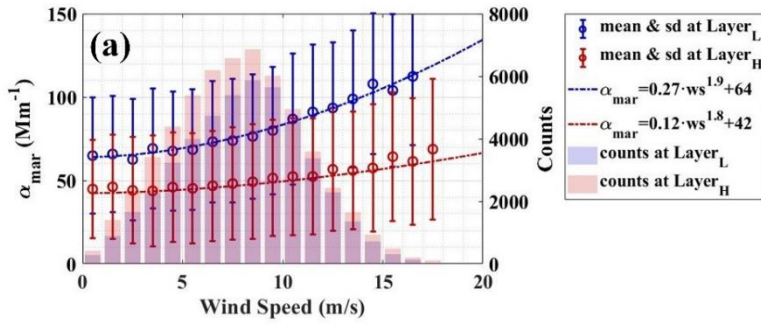
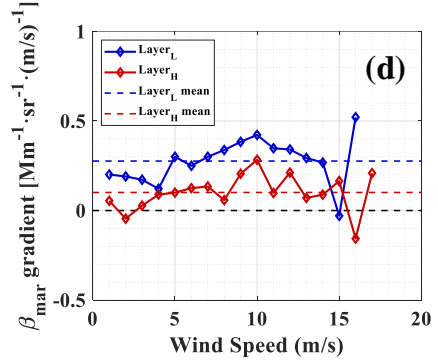
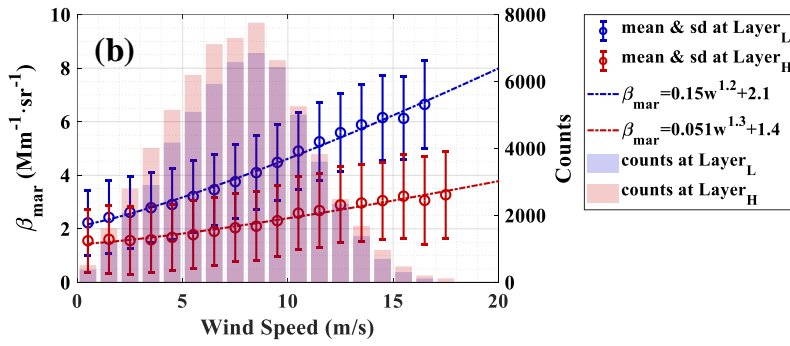
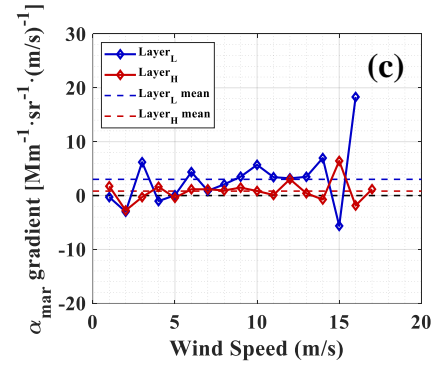
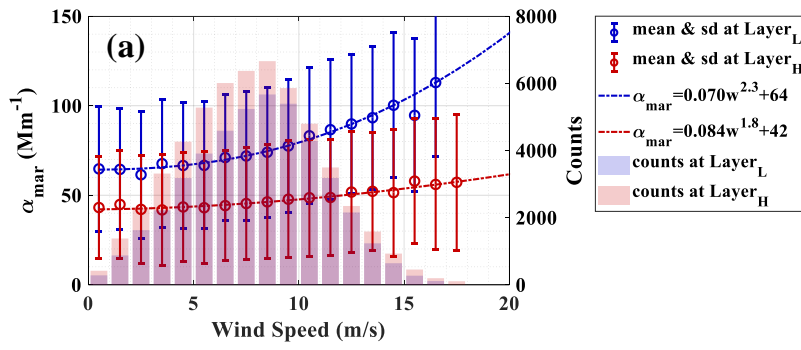
Table 1: Regression functions of the averaged optical properties and the wind speed grids, together with the corresponding wind speed distributions, grouped by areas and layers.

Area	Layer	Optical property	Regression function	R^2	Proportion of wind speed bins ($\text{m} \cdot \text{s}^{-1}$)			Number of counts
					$0 < ws \leq 8$	$8 < ws \leq 15$	$ws > 15$	
NP	H	α_{mar}	$\alpha_{mar} = 0.084 \cdot ws^{1.8} + 42$	0.9695	0.5253	0.46	0.0201	5575857545
		β_{mar}	$\beta_{mar} = 0.050 \cdot ws^{1.3} + 1.4$	0.976	0.5354	0.45	0.01	6419173870

L	α_{mar}	$\alpha_{mar} = 0.070 \cdot ws^{2.3} + 64$	<u>0.980.99</u>	<u>0.4849</u>	<u>0.5150</u>	0.01	<u>4485746854</u>
	β_{mar}	$\beta_{mar} = 0.15 \cdot ws^{1.2} + 2.1$	<u>1.00.99</u>	0.51	0.48	0.01	<u>5511763005</u>
H	α_{mar}	$\alpha_{mar} = 5.0 \cdot ws^{0.84} + 54$	0.95	0.46	0.34	0.20	<u>3408839999</u>
	β_{mar}	$\beta_{mar} = 1.3 \cdot ws^{0.48} + 1.1$	0.96	<u>0.4849</u>	0.31	<u>0.2120</u>	<u>3034839965</u>
SP	α_{mar}	$\alpha_{mar} = 6.1 \cdot ws^{0.83} + 73$	0.98	<u>0.4345</u>	0.38	<u>0.1917</u>	<u>2578330526</u>
	β_{mar}	$\beta_{mar} = 1.8 \cdot ws^{0.47} + 1.1$	0.97	<u>0.4547</u>	0.36	<u>0.1917</u>	<u>2385432375</u>
H	α_{mar}	$\alpha_{mar} = 0.65 \cdot ws^{1.4} + 56$	0.95	0.40	0.35	0.25	<u>1955224012</u>
	β_{mar}	$\beta_{mar} = 0.60 \cdot ws^{0.59} + 1.7$	0.96	<u>0.4042</u>	<u>0.3333</u>	<u>0.2725</u>	<u>1647322446</u>
SI	α_{mar}	$\alpha_{mar} = 1.1 \cdot ws^{1.2} + 81$	<u>0.9192</u>	<u>0.3638</u>	0.41	<u>0.2321</u>	<u>1595319489</u>
	β_{mar}	$\beta_{mar} = 1.2 \cdot ws^{0.47} + 1.7$	<u>0.9397</u>	<u>0.3646</u>	<u>0.4036</u>	<u>0.2418</u>	<u>1392319473</u>

Generally, in all cases shown in Fig. [118](#), Fig. [12-9](#) and Fig. [1310](#), the optical properties at Layer_L are all larger than those at Layer_H in the same wind speed grid, while the variations of marine aerosol optical properties along with wind speed grid can be clearly observed that the tendency is increasing with the wind speed. Moreover, the regression curves are fitted pretty well as the R^2 are all above 0.90.

465

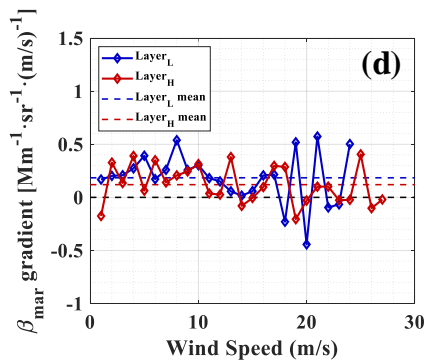
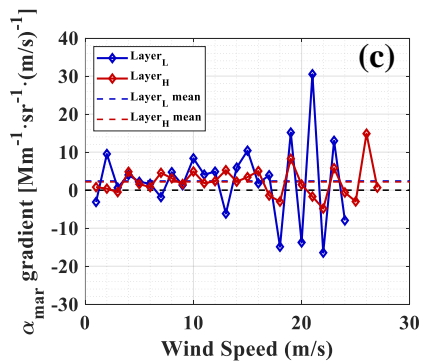
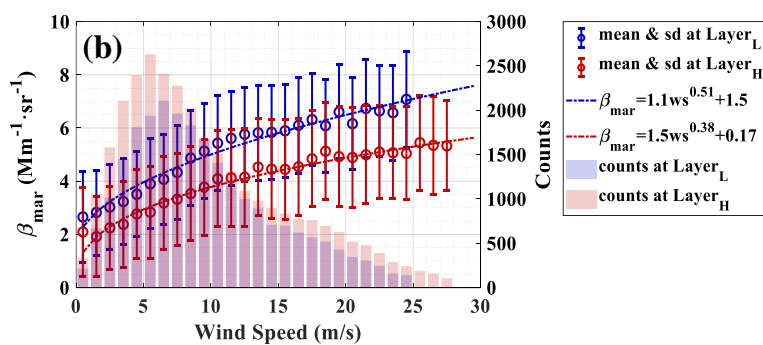
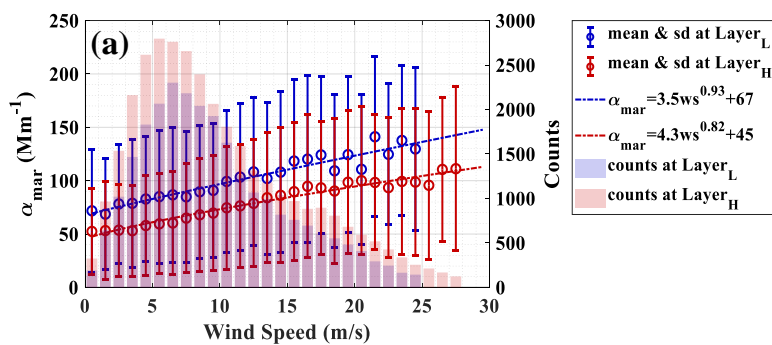
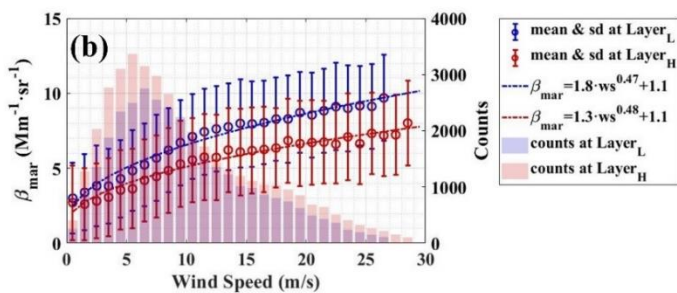
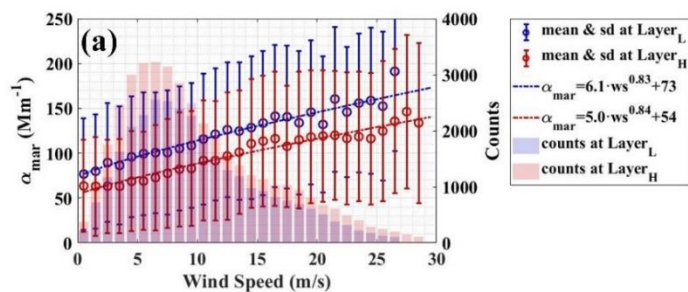


470 **Figure 148:** Relationship between marine aerosol optical properties ((a) for α_{mar} , (b) for β_{mar}) and wind speed above the NP area. The blue circles and error bars represent the means and standard deviations of the optical properties along wind speed grids at Layer_L, while the reds represent the same items at Layer_H. The blue and red dotted-dashed lines are the optical property averages regression curves fitted along the wind speed grid at Layer_L and Layer_H, respectively. The blue and red histograms indicate the data counts of every wind speed grid at Layer_L and Layer_H, respectively. (c) and (d) represent the gradients of α_{mar} and β_{mar} with wind speed at Layer_L (blue lines) and Layer_H (red lines), respectively, while the blue dashed lines and the red dashed lines show the mean values of the gradients at two layers.

475 It can be found from the panel (a) and (b) of Fig. 8. In the NP area, α_{mar} at Layer_L increases from 64 Mm⁻¹ at 0-1 m·s⁻¹ wind speed interval to 113 Mm⁻¹ at 16-17 m·s⁻¹ wind speed interval, while it at Layer_H increases from 42 Mm⁻¹ at 0-1 m·s⁻¹ wind speed interval to 57 Mm⁻¹ at 17-18 m·s⁻¹ wind speed interval; β_{mar} at Layer_L increases from 2.2 Mm⁻¹·sr⁻¹ at 0-1 m·s⁻¹ wind speed interval to 6.6 Mm⁻¹·sr⁻¹ at 16-17 m/s wind speed interval, while it at Layer_H increases from 1.6 Mm⁻¹·sr⁻¹ at 0-1 m·s⁻¹ wind speed interval to 3.3 Mm⁻¹·sr⁻¹ at 17-18 m/s wind speed interval. The increments of these two parameters at Layer_L are much larger than at Layer_H. Moreover, the exponents of the regression functions are all larger than 1, indicating the growth rates of the optical properties along the wind grid increases. Referring to the panel (c) and (d) of Fig. 8, the gradients' mean values of the α_{mar} and β_{mar} at Layer_L are higher than those at Layer_H. Besides, Within the same wind speed grid, the gradients at Layer_L is are mostly larger than that at Layer_H within the same wind speed interval, i.e., the optical

480 properties at Layer_L will increase more rapidly with wind speed. It is worth to notice that for the case that the wind speed is below above 15-10 m·s⁻¹, the gradients of β_{mar} ~~α_{mar}~~ and ~~seem to show decreasing tendencies~~ be fitted better by power law functions, whereas under the condition when the wind speed is higher lower than 15-10 m·s⁻¹, the values of the optical properties' gradients show higher fluctuations (~~α_{mar} β_{mar} at Layer_L~~) or are invariant (~~β_{mar} at Layer_H~~), deviating from the power laws present increasing tendencies, indicating the better fitting by power law functions at lower wind speed. It may result

490 from that the limited number of counts when the wind speed is larger than 15 m·s⁻¹, so that the statistical significance turns to be weak. This phenomenon may imply that However, the hypothesis could be discussed that there might be two distinct variation trends of β_{mar} the marine aerosol optical properties above or below the wind speed range of 15-10 m·s⁻¹.



495 **Figure 129:** Relationship between marine aerosol optical properties ((a) for α_{mar} , (b) for β_{mar}) and wind speed above the SP area. The items represent the same as those of Fig. 118.

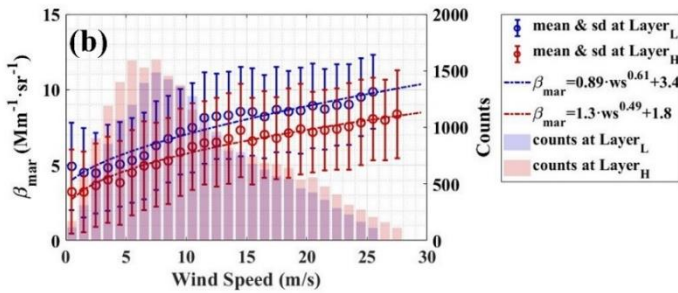
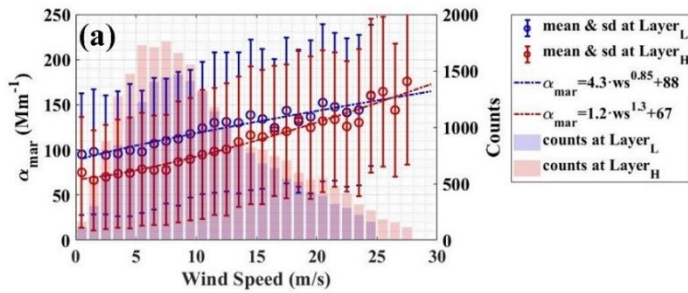
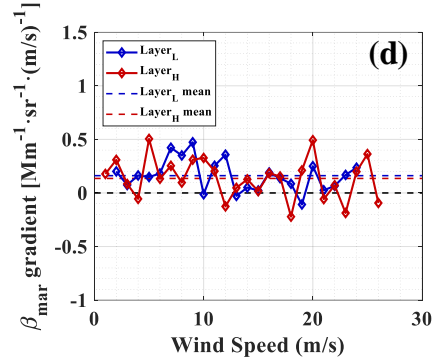
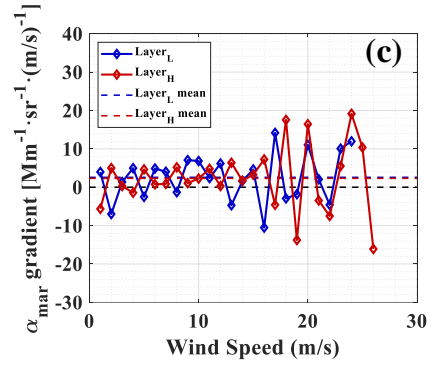
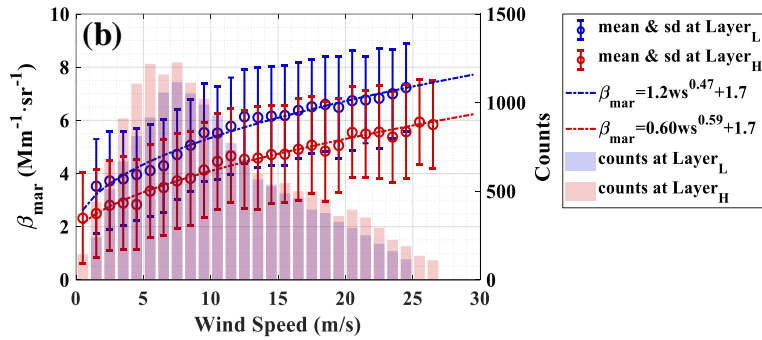
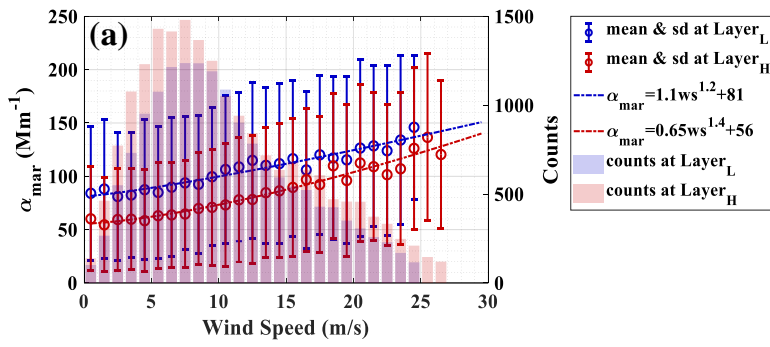


Figure 1310: Relationship between marine aerosol optical properties ((a) for α_{mar} , (b) for β_{mar}) and wind speed above the SI area.

500 The items represent the same as those of Fig. 118.

For the SP area and the SI area, ~~as mentioned above~~, the maximal wind speed can reach distribution ranges are larger, of which the maximum is up to 29-28 $\text{m} \cdot \text{s}^{-1}$, while the variations of the optical properties along with wind speed are more complicated. In Fig. 9 (a), ~~As for~~ the α_{mar} over the SP area, ~~they~~ show approximate linear growth tendencies with wind speed with similar gradients both at Layer_{L} and at Layer_{H} , with the fitting functions' exponents of 0.93 and 0.82 ~~when the wind speed is below~~ 17 $\text{m} \cdot \text{s}^{-1}$. The α_{mar} increase from 72 Mm^{-1} and 52 Mm^{-1} to 130 Mm^{-1} and 111 Mm^{-1} for Layer_{L} and Layer_{H} , respectively. Figure 9 (b) shows that the β_{mar} above the SP area increase from 2.7 $\text{Mm}^{-1} \cdot \text{sr}^{-1}$ and 2.1 $\text{Mm}^{-1} \cdot \text{sr}^{-1}$ to 7.0 $\text{Mm}^{-1} \cdot \text{sr}^{-1}$ and 5.3 $\text{Mm}^{-1} \cdot \text{sr}^{-1}$, with the fitting functions' exponents of 0.51 and 0.38 for Layer_{L} and Layer_{H} . From Fig. 10 (a) and (b), it can be found that the variations of α_{mar} and β_{mar} with wind speed in the SI area are similar to those in the SP area, except for that the fitting functions' exponents of β_{mar} are larger than 1, which are 1.2 and 1.4 for Layer_{L} and Layer_{H} , respectively. In the Layer_{H} of SI area, α_{mar} at above 25 $\text{m} \cdot \text{s}^{-1}$ can reach up to 137 Mm^{-1} , much larger than that of around 110 Mm^{-1} in the SP area. The panel (c) and (d) of Fig. 9 and Fig. 10 show the gradients of α_{mar} and β_{mar} with the wind speed above the SP area and the SI area. In these four panels, the blue dashed lines (gradients' mean values at Layer_{L}) are all higher than the red lines (gradients' mean values at Layer_{H}), illustrating that the increments of α_{mar} and β_{mar} per unit wind speed at Layer_{L} are larger than those at Layer_{H} , which implies that the input of marine aerosol driven by wind at Layer_{L} is stronger than at Layer_{H} . Focusing on the panel (c) of Fig. 9 and Fig. 10, it can be seen that, for both layers of the SP area and the SI area, the gradients of α_{mar} below 15 $\text{m} \cdot \text{s}^{-1}$ are almost all larger than 0 fluctuating slightly around the mean values, while the gradients of α_{mar} above 15 $\text{m} \cdot \text{s}^{-1}$ fluctuate drastically around 0. This phenomenon may indicate that below 15 $\text{m} \cdot \text{s}^{-1}$, both layers continually receive the input of marine aerosol driven by wind, nevertheless when the wind speed is higher than 15 $\text{m} \cdot \text{s}^{-1}$, the dependency of marine aerosol on wind become lower. As for the gradients of β_{mar} above the SP area and the SI area, from the panel (d) of Fig. 9 and Fig. 10, it can be found obviously that for both layers, the gradients of β_{mar} decrease above around 10 $\text{m} \cdot \text{s}^{-1}$. The corresponding variations of β_{mar} above the SP area and the SI area are shown in the panel (b) of Fig. 9 and Fig. 10, of which the β_{mar} increase with higher slopes at the wind speed range of 0-10 $\text{m} \cdot \text{s}^{-1}$ while the slopes of the increasing become lower when the wind speed is above 10 $\text{m} \cdot \text{s}^{-1}$. This phenomenon might indicate that the increasing of β_{mar} with wind speed includes two separate trends regarding 10 $\text{m} \cdot \text{s}^{-1}$ as the change point, consist with the surmise raised in the analysis of the NP area.

When the wind speeds exceed 17 $\text{m} \cdot \text{s}^{-1}$, the growth rates of α_{mar} become smaller with several fluctuating values. The change point of the gradient can also be discovered in the variations of β_{mar} , which is approximately 12 $\text{m} \cdot \text{s}^{-1}$ for the both layers. Regardless of below the gradient change point or above it, the growth rate of β_{mar} at Layer_{L} is higher than that at Layer_{H} . In

530 the SI area, the variations of the optical properties along with the wind speed grid are similar to those in the SP area. The gradients of α_{mar} are quite similar to each other at both layers while the growth rate of β_{mar} at the lower layer is larger than that at the higher layer. The change points of the gradient also exist at around $15 \text{ m}\cdot\text{s}^{-1}$ and at around $12 \text{ m}\cdot\text{s}^{-1}$, for Layer_L and Layer_H respectively. However, it is noticed that some optical property values at the wind speed of $1 \text{ m}\cdot\text{s}^{-1}$ to $5 \text{ m}\cdot\text{s}^{-1}$ in the SI area are larger than those in the SP area, further the invariability or even the decrease occur at this wind speed bin. It is worth to note that under quite high wind speed condition ($24 \text{ m}\cdot\text{s}^{-1}$ to $28 \text{ m}\cdot\text{s}^{-1}$), the α_{mar} values at Layer_H in the SI area
535 enhance sharply, resulting in an exponent above 1. It indicates that after the slow growth phase of the α_{mar} in the wind speed bins of $15 \text{ m}\cdot\text{s}^{-1}$ to $24 \text{ m}\cdot\text{s}^{-1}$, α_{mar} will still increase significantly. The same phenomenon can be observed at Layer_H in the SP area. Nevertheless, this rapid enhancement of α_{mar} is not possible to be observed at Layer_L, which is caused by an insufficient low number of counts for high wind speeds. n. This phenomenon is also not shown in the β_{mar} variations at high wind speed in both areas, as the variation trends of β_{mar} at high wind speed present similar gradients with those at the slow growth phase.
540 Consequently, for all of the measurement cases, and identical wind speed bins, the marine aerosol optical properties at Layer_L are larger than those at Layer_H in any identical wind speed interval, indicating that the MABL possibly receive more marine aerosol produced and transport from the air-sea interface, while the higher layer above the MABL with the upper boundary of 2 km can also be influenced by the marine aerosol but less. ~~In the NP area, the variations of the marine aerosol optical properties with the relatively concentrated wind speed distribution are all fitted quite well by a power law functions of with the exponents above 1.~~ The gradients' mean values of α_{mar} and β_{mar} gradients at Layer_L are obviously all larger than at Layer_H ~~for the same wind speed~~, which implies that the marine aerosol enhancements caused by the background wind are ~~much~~ more intensive at the MABL. ~~In the SP area and the SI area, the enhancement rates of the marine aerosol optical properties at both layers are similar with the large wind speed bins up to $29 \text{ m}\cdot\text{s}^{-1}$, which indicates that the marine aerosol evolution of both atmospheric layers over the ocean will be affected by the background wind.~~ It should be emphasized that the gradients change points appear
545 during the growth of α_{mar} and β_{mar} the optical properties along with wind speed ~~in these two areas~~. The gradient change points of α_{mar} ($15 \text{ m}\cdot\text{s}^{-1}$) ~~are is~~ greater than ~~those that~~ of β_{mar} ($10 \text{ m}\cdot\text{s}^{-1}$), and above them the enhancement rate becomes lower. It might illustrate that the enhancement of marine aerosol driven by wind includes two phases, among them one is growing rapidly phase with high dependency of wind, and another is after the gradient change points, the marine aerosol enhancement by wind is likely to diminish ~~with the wind speed increasing~~. The possible sharp increase of α_{mar} at Layer_H under high wind
555 speed condition ($24 \text{ m}\cdot\text{s}^{-1}$ to $28 \text{ m}\cdot\text{s}^{-1}$) is worth to notice as well.

In this section, histograms for the marine aerosol optical properties at 355 nm versus the wind speed with α_{mar} -WS grid and β_{mar} -WS grid at two separate atmospheric layers are discussed. Then the statistical results of the marine aerosol optical properties at 355 nm along with the wind speed grid at two layers together with the corresponding regression curves are determined and analysed. It is found that both the MABL and the higher layer above the MABL can receive the marine aerosol produced and transported from air-sea interface. Moreover, the marine aerosol load at the lower layer (MABL) is stronger than at the higher layer. The marine aerosol shows enhancement when the wind speed is increasing, indicating that the wind performs as a significant factor for the marine aerosol at these layers. The wind speed bins and the marine aerosol variation tendencies with wind speed at these vertical layers above the individual study areas (the NP area, located in the Pacific Ocean, the low latitudes of the Northern Hemisphere; the SP area, located in the Pacific Ocean, the middle latitudes of the Southern Hemisphere; the SI area, located in the Indian Ocean, the middle latitudes of the Southern Hemisphere) are different from each other. It implies that the development and evolution of the marine aerosol above the ocean might not only be dominated by the driving of the wind, but also be impacted by other factors. That is to say, as concluded in Lewis and Schwartz (2004), apart from wind, there are some other meteorological and environmental factors, e.g. atmospheric stability, sea and air temperature, RH and so on, that are capable of affecting marine aerosol production, entrainment, transport and removal.

570 4.4 Dependency of aerosol optical depth and lidar ratio with wind speed

4.4.1 Marine aerosol optical depth vs. wind speed

As introduced in Section 1 of this paper, almost all the previous researches on the relationship between marine aerosol's optical properties and wind speed focused on the AOD of marine aerosol. In this study, as well, the effort-attempt on the averaged 0-2 km AOD_{mar} of individual wind speed grid calculation has been conducted to compare the AOD_{mar} -WS relationship from previous study. The AOD_{mar} of every single profile is acquired by integrating Aeolus retrieved α_{mar} within 2 km. The wind speed profiles are also averaged for 2 km to correspond to the AOD_{mar} data. Then the relationship between the AOD_{mar} and the wind speeds is obtained by averaging the AOD_{mar} in each wind speed grid-interval ($0 \text{ m}\cdot\text{s}^{-1}$ - $30 \text{ m}\cdot\text{s}^{-1}$, stepped by $1 \text{ m}\cdot\text{s}^{-1}$). The AOD_{mar} -WS relationship is also explored utilizing the products from the A-Train satellites (Kiliyanpilakkil and Meskhidze, 2011). "clean marine" aerosol AOD at 532 nm above ocean surface (up to 2 km) provided by CALIOP and 10 m daily wind speed provided by AMSR-E were used. It should be noticed that the wind speed used in Kiliyanpilakkil and Meskhidze (2011) is daily ocean surface wind speed, different from that in this study, which is instantaneous layer-averaged wind speed. Collecting the data for the time period from 2006 to 2011 over 15 remote ocean regions globally, the regression curve of is acquired with the averaged AOD_{mar} at 532 nm for each wind speed grid and the surface wind speed which is up to $29 \text{ m}\cdot\text{s}^{-1}$, and the regression function is shown as the following Eq. 3:

$$585 \quad \text{AOD}_{\text{mar},532} = \frac{0.15}{1 + 6.7 \cdot e^{-0.17 \cdot U_{10}}}, \quad (3)$$

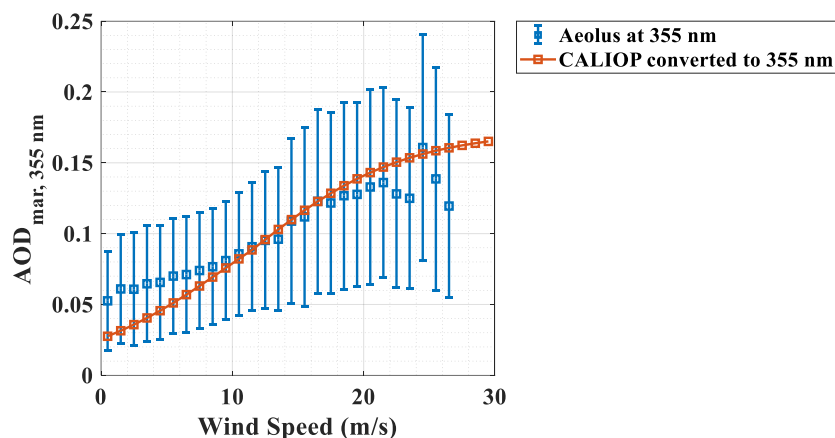
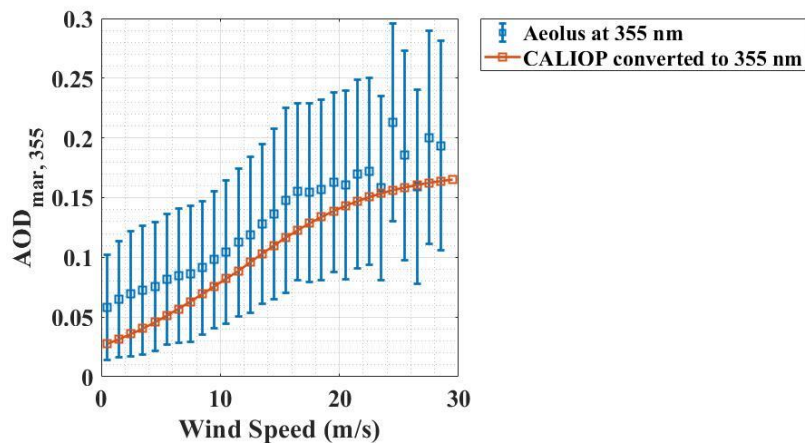
where the U_{10} represents daily 10 m ocean surface wind speed.

As described above, the AOD_{mar} data source (from spaceborne lidar observation), the study areas (remote ocean regions globally), and the wind speed range ($0 \text{ m} \cdot \text{s}^{-1}$ - $29 \text{ m} \cdot \text{s}^{-1}$) of the AOD_{mar} - ws relationship exploration in Kiliyanpilakkil and Meskhidze (2011) ~~are all quite similar~~ match well with those of this study. Hence, we select the AOD_{mar} - ws relationship established by Kiliyanpilakkil and Meskhidze (2011) for the comparison. Additionally, due to the different wavelengths of AOD_{mar} used in this study (355 nm) and in Kiliyanpilakkil and Meskhidze (2011) (532 nm), the effort on conversion of the AOD_{mar} at 532 nm to the AOD_{mar} at 355 nm is performed by applying the typical Ångström exponent of marine aerosol. It is reported that the marine aerosol Ångström exponent is surface wind speed related, and a linear relationship was established as the following Eq. 4 (Sayer et al., 2012):

$$595 \quad A(ws) = 0.69 - 0.030 \cdot ws, \quad (4)$$

where A represents the Ångström exponent and ws represents the wind speed. Then the AOD_{mar} at 532 nm can be converted to the AOD_{mar} at 355 nm by the following Eq. 5:

$$\text{AOD}_{\text{mar},355\text{nm}}(ws) = \exp\left[A(ws) \cdot \ln \frac{532}{355}\right] \cdot \text{AOD}_{\text{mar},532\text{nm}}(ws). \quad (5)$$



600

Figure 1411: AOD_{mar} at 355 nm versus wind speed. The blue squares and the corresponding error bars represent the AOD_{mar} means and standard deviations along the ws grid of all the three study areas in this study; the red squares and line represent the AOD_{mar} at 355 nm along the ws grid converted from the regressive relationship between the AOD_{mar} at 532 nm and the ocean surface wind speed reported by Kiliyanpilakkil and Meskhidze (2011).

605

In Fig. 1411, the averaged AOD_{mar} and the corresponding standard deviations at 355 nm of all three study areas along the wind speed grid are represented as the blue squares and the error bars, while the regression curve of AOD_{mar} at 355 nm versus wind speed converted from Eq. 3 are represented as the red squares and line. Although instantaneous layer-averaged wind speed ~~from ECMWF model~~ and daily ocean surface wind speed are used in this study and in Kiliyanpilakkil and Meskhidze (2011) individually, quite-similar tendency of AOD_{mar} at 355 nm versus wind speed are obtained. It can be found that AOD_{mar}

610

is increasing with wind speed, and the gradient of AOD_{mar} turns out becoming higher along the wind speed ~~grids~~ when the wind speed is below $15 \text{ m}\cdot\text{s}^{-1}$ while the variation of AOD_{mar} becomes ~~lower-slower~~ above $15 \text{ m}\cdot\text{s}^{-1}$. The converted CALIOP AOD_{mar} are ~~all slightly~~ lower than the Aeolus retrieved AOD_{mar} at 0-10 $\text{m}\cdot\text{s}^{-1}$, nevertheless the formers are all in

the standard deviations range of the latter, thus it is considered that the Aeolus retrieved AOD_{mar} and their variation along the wind speed are reasonable. The lower AOD_{mar} from CALIOP after wavelength conversion at low wind speed may arise from using a fixed LR_{mar} lidar ratio of 20 sr at 532 nm used for CALIOP AOD_{mar} retrievals while the LR_{mar} lidar ratio of marine aerosol can vary with the particle size a quite large range of 10 sr to 90 sr (Masonis et al., 2003). Possible uncertainties underestimation of the CALIOP retrieved AOD_{mar} at 532 nm is discussed in detail in Kiliyanpilakkil and Meskhidze (2011). Besides, as discussed in Section 4.4.2 of this paper, the particle size of marine aerosol and the lidar ratio LR_{mar} of the marine aerosol will vary with wind speed, so using the CALIOP AOD_{mar} retrieved with the fixed LR_{mar} lidar ratio may generate additional error in the exploration of the relationship between the AOD_{mar} and the wind speed. Therefore, using Aeolus retrieved AOD_{mar} , which is integrated by independently retrieved extinction coefficient without the assumption of LR_{mar} lidar ratio, could make the AOD_{mar} - w/s relationship more reliable. ~~The slightly high Aeolus retrieved AOD_{mar} may result from the possible cloud contaminations of the marine aerosol data bins.~~

4.4.2 Marine aerosol lidar ratio vs. wind speed

~~Derived from α_{mar} and β_{mar} , LR_{mar} is defined as the ratio of the former to the latter.~~ As one of the intensive optical properties, LR_{mar} ~~it is~~ independent of the aerosol concentration. It is reported that the LR_{mar} depends on the particle size, and specifically, with the reduction of the coarse mode, the total lidar ratio LR turns out to increase (Masonis et al., 2003). The possible reason for this phenomenon is that as the particles become smaller, the extinction is enhanced by the increasing sideward scattering and the backscatter gets weaker due to the decrease of the scattering cross section (Haarig et al., 2017). Aeolus L2A product provide particle extinction-to-backscatter ratio calculated with the raw β backscatter coefficient, which lacks the depolarized portion, as introduced in Section 3 of this paper. In this work, the corrected LR_{mar} marine aerosol lidar ratio is acquired by dividing the marine aerosol extinction to the marine aerosol depolarization-corrected backscatter. The calculation of the averaged LR_{mar} along wind speed grid has been conducted by averaging the LR_{mar} marine aerosol lidar ratios of each $1 \text{ m} \cdot \text{s}^{-1}$ wind speed bin, meanwhile the standard deviations are acquired as well. It should be noted that before the statistical calculation, the outliers are eliminated by the method of Tukey's test, which is introduced in Section 3 of this paper.

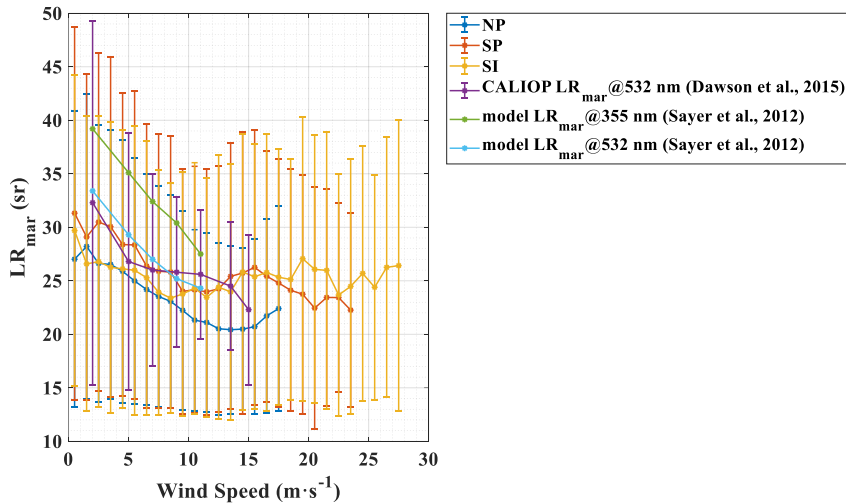
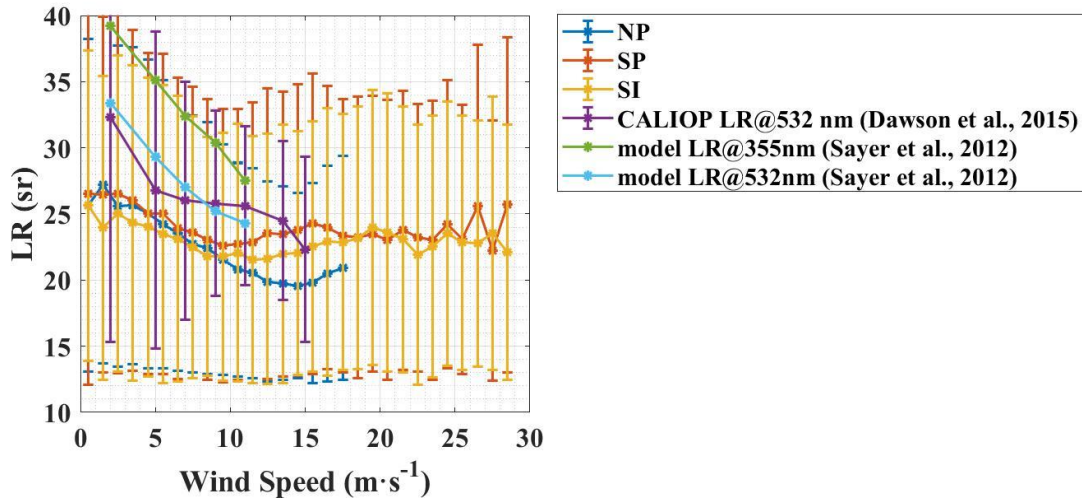
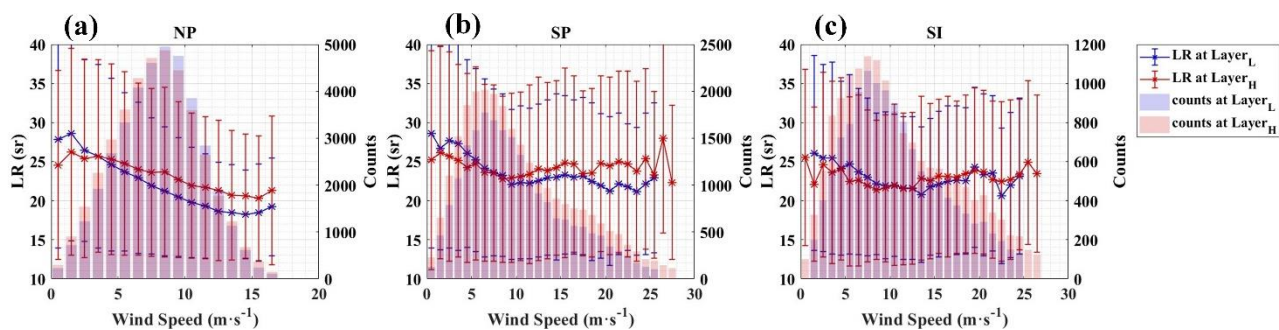


Figure 1512: LR_{mar} versus the wind speed. The dark blue curve, red curve, yellow curve and the corresponding error bars represent the averaged LR_{mar} and their standard deviations above the NP area, the SP area and the SI area, respectively. The purple curve and the corresponding error bars represent the CALIOP-retrieved LR_{mar} at 532 nm (Dawson et al., 2015). The green curve and the light blue curve represent the modelled LR_{mar} at 355 nm and at 532 nm, respectively (Sayer et al., 2012).

In Fig. 1512, 0-2 km averaged LR_{mar} variations along with the wind speed above the NP area, the SP area and the SI area are represented as the blue curve, the red curve and the yellow curve, respectively. Generally, the distinct downward trend of the LR_{mar} at relatively low wind speeds (0-15-14 $\text{m}\cdot\text{s}^{-1}$ of the NP area, 0-10-9 $\text{m}\cdot\text{s}^{-1}$ of the SP area and 0-10 $\text{m}\cdot\text{s}^{-1}$ of the SI area) can be observed in all cases. The similar results reported in this paper are similar to those in the previous studies, of which Dawson et al. (2015) and Sayer et al. (2012) investigated the relationship between LR_{mar} and wind speed utilizing measured

~~LR_{mar} and modelled LR_{mar} respectively have been investigated with the measured LR_{mar} or modelled LR_{mar} and the ocean surface wind speed in the previous studies.~~ Combining the corrected CALIOP-retrieved LR_{mar} at 532 nm and 10 m ocean surface wind speed from the ~~Advanced Microwave Scanning Radiometer (AMSR-E)~~, the negative correlation between the LR_{mar} and wind speed is acquired with the wind speed bins of 0 m·s⁻¹ up to >15 m·s⁻¹, shown as the purple curve in Fig. ~~45-12~~ (Dawson et al., 2015). The modelled LR_{mar} at 355 nm and at 532 nm also presents decreasing trends with the wind speed increases, presented as the green curve and the light blue curve in Fig. ~~45-12~~ (Sayer et al., 2012). These results seem to imply that as the wind speed increases for a low wind speed range, the particle size of marine aerosol get larger. The phenomenon is explained by the shift in marine aerosol volume size distribution with wind speed as wind speed increases, the fine mode volume size distribution of marine aerosol turns out decline while the coarse mode distribution becomes larger (Dawson et al., 2015; Smirnov et al., 2003; Sayer et al., 2012). The CALIOP LR_{mar} and the modelled LR_{mar} are all larger than the LR_{mar} of this study but are all in the standard deviation ranges. According to ~~Bohlmann et al. (2018)~~, Groß et al. (2011), Groß et al. (2015), ~~Bohlmann et al. (2018)~~ and Floutsi et al. (~~2022~~2023), the pure LR_{mar} at 355 nm can vary from 10 sr to 40 sr, thus it is considered that the averaged LR_{mar} in this study are reasonable. At the middle wind speed range (~~15-14~~ m·s⁻¹ -18 m·s⁻¹ of the NP area, ~~10-9~~ m·s⁻¹ -16 m·s⁻¹ of the SP area, 10 m·s⁻¹ -20 m·s⁻¹ of the SI area), the LR_{mar} show upward tendencies, implying that the marine aerosol particles might be broken up into smaller ones with a wind speed increase. At the very high wind speed (~~16~~ m·s⁻¹) above the SP area (>16 m·s⁻¹) and the SI area (>20 m·s⁻¹), the LR_{mar} ~~marine aerosol particle size variations~~ turns out to a stable state along decreasing with the wind speed again, which indicates that the particle size of marine aerosol becomes larger at this wind speed condition.



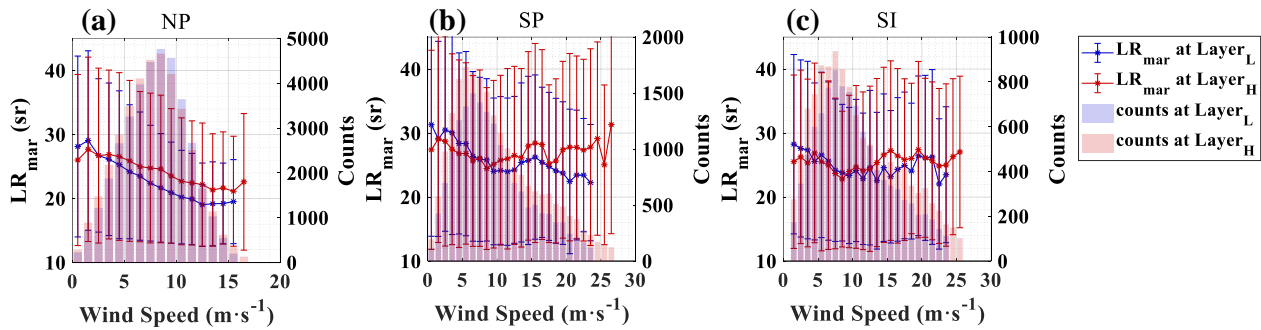


Figure 1613: Averaged LR_{mar} versus wind speed at Layer_L and Layer_H , in (a) the NP area, (b) the SP area and (c) the SI area, respectively.

670 ~~The LR_{mar} of two separate vertical layers are also calculated and discussed. Figure 16-13 shows the LR_{mar} variations at Layer_L and Layer_H along with the wind speed grid in three study areas. Some divergences of the LR_{mar} variations between the layers can be discovered. As for the NP area, the variation of LR_{mar} at Layer_L is from 29 sr at 1-2 $\text{m}\cdot\text{s}^{-1}$ to 19 sr at 12-13 $\text{m}\cdot\text{s}^{-1}$, larger than that at Layer_H , which is from 28 sr at 1-2 $\text{m}\cdot\text{s}^{-1}$ to 21 sr at 15-16 $\text{m}\cdot\text{s}^{-1}$. Regarding to the SP area and the SI area, the downward trend of LR_{mar} at high wind speed condition as mentioned above is not apparent at Layer_H . Moreover, at Layer_H , the LR_{mar} can reach up to 27-28 sr at 15-25 $\text{m}\cdot\text{s}^{-1}$, close to that at 0-5 $\text{m}\cdot\text{s}^{-1}$, implying that the marine aerosol particle sizes at low and high wind speed are similar. In all the three study areas, the particle size of marine aerosol at Layer_L is likely to vary from smaller than at Layer_H to bigger than at Layer_H when the wind speed increases. During the LR_{mar} decreasing phase along with the wind speed, it is indicated that the variations of the particle size at Layer_L are larger than those at Layer_H .~~

675

Generally, the LR_{mar} dependency along with the wind speed shows a downward trend at relatively low wind speed, then an upward trend at the middle wind speed, finally again a downward-stable at the very high wind speed (if exist), which implies that the marine aerosol particle size is increasing along with the wind speed at first, then might be broken up into smaller one by the enhanced wind speed and ultimately turns out to a stable larger-size again. Several differences of the LR_{mar} variations along with the wind speed appear between the three study areas and the two vertical layers, which may be due to the differences in meteorological and environmental conditions of the areas and the layers.

680

685 5 Summary and conclusion

By utilizing Level 2A products (particle optical properties and numerical weather prediction data) and Level 2C products (numerical weather prediction wind vector assimilated with observed wind component) provided by ALADIN, and L2 vertical

feature mask (VFM) products provided by CALIOP, the optical properties at 355 nm of pure marine aerosol are derived. Then the combined analysis of marine aerosol optical properties at 355 nm and instantaneous co-located wind speed ~~from ECMWF model~~ above remote ocean areas is conducted. Finally, their relationships are explored and discussed at two separate vertical atmospheric layers ($Layer_L$ with the height of 0-1 km and $Layer_H$ with the height of 1-2 km, correspond to the heights within and above marine atmospheric boundary layer (MABL)), revealing the marine aerosol related atmospheric background states within and above the MABL over the remote oceans.

Three study areas located in remote ocean were selected, which were named the North Pacific (NP) area, the South Pacific (SP) area and the South Indian (SI) area, respectively. Pure marine aerosol is identified by distinguishing marine aerosol from other aerosols and from clouds. The areas selected procedure in this work includes selecting the ocean areas far away from the lands, checking the potential of terrestrial aerosol input by analysing the wind direction of the selected areas, and then we examining-examined the domination of marine aerosol with the aerosol classification data provided by CALIOP VFM products. The proportions of marine aerosol in these three areas are all larger than 79% respectively while the percentage sums of marine aerosol and dusty marine aerosol are all above 90%. After quality control, cloud screening was conducted with the criteria (relative humidity and backscatter ratio), and 9%, 35%, 40% data was identified cloud contaminated in the altitude range of 0-2 km then was eliminated for the NP area, the SP area and the SI area, respectively, and Finally, backscatter-backscatter correction is applied to the Aeolus L2A products, this-These procedures allow us to obtain reliable, cloud-free marine aerosol optical properties and the corresponding wind speed.

~~The spatial distributions of marine aerosol optical properties and wind speed above the North Pacific (NP) area, the South Pacific (SP) area and the South Indian (SI) area are respectively presented and analysed within and above the marine atmospheric boundary layer. The results show, since the three study areas are located in different hemispheres, different latitudes and different oceans, that the spatial distributions of wind speed (ws), marine aerosol extinction coefficient (α_{mar}), marine aerosol backscatter coefficient (β_{mar}) and marine aerosol lidar ratio (LR_{mar}) are not totally similar. Nevertheless, the marine aerosol optical properties and the wind speed show positive correlation both over $Layer_L$ $Layer_H$ and $Layer_L$ $Layer_H$, whereas the optical properties at $Layer_L$ are larger than those at $Layer_H$, indicating that both layers are affected by marine aerosol produced and transported from air-sea interface but the majority of the marine aerosol is trapped in the MABL while a small fraction can be elevated into the higher layer above the MABL.~~

The statistical results of the marine aerosol optical properties (extinction coefficient (α_{mar}) and backscatter coefficient (β_{mar})) at 355 nm with the wind speed (ws) are analysed at 355 nm along with the wind speed grid at $Layer_L$ and $Layer_H$ for three study areas respectively at two vertical layers together with the corresponding regression curves fitted by power-law functions are acquired and analysed, for three study areas respectively. It is found that both the MABL and the higher layer above the MABL can receive the marine aerosol produced and transported from air-sea interface. Moreover, the marine aerosol load at the lower layer (MABL) is stronger than at the higher layer. The marine aerosol enhancements caused by the background wind

720 are more intensive at the MABL. Besides, the gradient change points of α_{mar} ($15 \text{ m} \cdot \text{s}^{-1}$) and of β_{mar} ($10 \text{ m} \cdot \text{s}^{-1}$) were found
during the growth of α_{mar} and β_{mar} with wind speed, above which the growth rate of α_{mar} and β_{mar} becomes lower. It might
illustrate that the enhancement of marine aerosol driven by wind includes two phases, among which one is growing rapidly
phase with high dependency of wind, and another is after the gradient change points, the marine aerosol enhancement by wind
is likely to diminish. The $\alpha_{mar} - ws$ curves and the $\beta_{mar} - ws$ curves were fitted by power law functions and the corresponding
725 R^2 are all higher than 0.9 for both layers above all three study areas. Regarding to the derived data, The optical properties
present increasing trends with wind speed in all cases. As for the NP area, the gradients of the optical properties at Layer_L are
higher than at Layer_H in the identical wind speed grid, illustrating that the marine aerosol enhancement caused by the
background wind are much more intensive in the MABL. The exponents of all the regression functions are above 1, which
indicates that the growth rates of the optical properties with wind speed become larger. In aspect of the SP area and the SI area,
730 the growth rates of the marine aerosol optical properties at both layers are similar, which reveals that the marine aerosol
evolution within or above the MABL over ocean will be affected by the background wind. The gradient change points appear
during the growth of the optical properties along wind speed, above which the growth rate turns out lower, implying that after
the gradient change points, the marine aerosol enhancement is likely to diminish with the wind speed increasing. Compared
with the regression function between wavelength-converted CALIOP-retrieved AOD_{mar} and 10 m surface wind speed, the
735 AOD_{mar} at 355 nm versus the wind speed in this work shows quite consistent tendency with CALIOP's though the wind
speeds used are different. The LR_{mar} depends on the and marine aerosol particle size have negative relationship (Masonis et
al., 2003). The From the relationship between the LR_{mar} and the wind speed, are also explored and discussed, it indicatesing
that as the wind speed is increasing, the particle size of marine aerosol obviously becomes larger at relative low wind speed
range, then could be broken up into smaller -by wind at higher wind speed, and ultimately turns out a stable-larger size-state
740 again at very high wind speed.
The $\alpha_{mar} - ws$ and $\beta_{mar} - ws$ models within and above MABL at remote ocean areas were established with Aeolus provided data.
Nevertheless, the regression curves of $\alpha_{mar} - ws$ and $\beta_{mar} - ws$ above three study areas (the NP area, located in the Pacific
Ocean, the low latitudes of the Northern Hemisphere; the SP area, located in the Pacific Ocean, the middle latitudes of the
Southern Hemisphere; the SI area, located in the Indian Ocean, the middle latitudes of the Southern Hemisphere) are not totally
745 consistent, while the meteorological and environmental conditions apart from wind are also distinct at different regions. It
implies that in order to obtain more precise α_{mar} and β_{mar} models, besides wind speed, other meteorological and environmental
factors, e.g., atmospheric stability, sea and air temperature, RH, etc. should participate in the establishment of the models,
because the production, entrainment, transport and removal of the marine aerosol above the ocean are not only dominated by
the wind, but also be impacted by these factors (Lewis and Schwartz, 2004). To conclude, this study derived pure marine
750 aerosol-optical properties and the corresponding wind speed, explored the relationship between these two elements, revealing

755 ~~the marine aerosol related atmospheric background states at two separate layers within and above the MABL over the remote~~
~~oceans. The atmosphere of the two vertical layers over the ocean areas will both receive the marine aerosol input produced~~
~~and transported by the wind and the turbulence. The marine aerosol enhancement caused by the wind speed in the MABL is~~
~~more intensive than at the higher layer. The marine aerosol optical properties distributions, wind speed bins, and the marine~~
~~aerosol variation tendencies along wind speed grid above the individual study areas are not totally similar. It can be inferred~~
~~that the development and evolution of the marine aerosol above the ocean might not only be dominated by the wind, but also~~
~~be impacted by other meteorological and environmental factors, e.g. atmospheric stability, sea and air temperature, RH and so~~
~~on.~~ If future study is capable to obtain more other meteorological parameters above ocean, jointly analysing the aerosol optical
760 properties and the wind together with them, more detailed information of marine aerosol production, entrainment, transport
and removal will be acquired.

Data availability

The Aeolus data are downloaded via the website <https://aeolus-ds.eo.esa.int/oads/access/collection> (last access: 9 March 2023).
Part of the Aeolus L2A and L2C data we used in this paper are not available publicly at the time the article was submitted. We
are allowed to access the data through our participation as a Calibration and Validation team. The CALIOP data can be
765 downloaded from <https://eosweb.larc.nasa.gov/project/CALIPSO> (last access: 9 March 2023).

Author contributions

G. Dai conceived of the idea for correlation between marine aerosol optical properties and wind fields over remote oceans with
spaceborne lidars ALADIN, CALIOP; K. Sun wrote the manuscript; K. Sun, G. Dai, S. Wu, O. Reitebuch and H. Baars
contributed to the data analyses; J. Liu and S. Zhang contributed to the scientific discussion. All the co-authors reviewed and
770 edited the manuscript.

Competing interests

The authors declare that they have no conflict of interest.

Special issue statement

This article is part of the special issue “Aeolus data and their application”. It is not associated with a conference.

775 **Acknowledgments**

This study has been jointly supported by the Laoshan Laboratory Science and Technology Innovation Projects under grant LSKJ202201406, the National Natural Science Foundation of China (NSFC) under grant 61975191, 41905022 and U2106210. This work was also supported by Dragon 5 program which conducted by European Space Agency (ESA) and the National Remote Sensing Center of China (NRSCC) under grant 59089.

780 **References**

- Abril-Gago, J., Guerrero-Rascado, J. L., Costa, M. J., Bravo-Aranda, J. A., Sicard, M., Bermejo-Pantaleón, D., Bortoli, D., Granados-Muñoz, M. J., Rodríguez-Gómez, A., Muñoz-Porcar, C., Comerón, A., Ortiz-Amezcuca, P., Salgueiro, V., Jiménez-Martín, M. M., and Alados-Arboledas, L.: Statistical validation of Aeolus L2A particle backscatter coefficient retrievals over ACTRIS/EARLINET stations on the Iberian Peninsula, *Atmos. Chem. Phys.*, 22, 1425–1451, <https://doi.org/10.5194/acp-22-1425-2022>, 2022.
- Adames, A. F., Reynolds, M., Smirnov, A., Covert, D. S., and Ackerman, T. P.: Comparison of MODIS ocean aerosol retrievals with ship-based sun photometer measurements from the “Around the America’s” expedition, *J. Geophys. Res.*, 116, D16303, <https://doi.org/10.1029/2010JD015440>, 2011.
- Alexander, S. P. and Protat, A.: Vertical profiling of aerosols with a combined Raman-elastic backscatter lidar in the remote Southern Ocean marine boundary layer (43–66°S, 132–150°E), *J. Geophys. Res.-Atmos.*, 124, 12107–12125, <https://doi.org/10.1029/2019JD030628>, 2019.
- Ansmann, A., Wandinger, U., Le Rille, O., Lajas, D., and Straume, A. G.: Particle backscatter and extinction profiling with the spaceborne high-spectral-resolution Doppler lidar ALADIN: methodology and simulations, *Appl. Optics*, 46, 6606, <https://doi.org/10.1364/AO.46.006606>, 2007.
- Baars, H., Radenz, M., Floutsi, A. A., Engelmann, R., Althausen, D., Heese, B., Ansmann, A., Flament, T., Dabas, A., Trajon, D., Reitebuch, O., Bley, S., and Wandinger, U.: Californian wildfire smoke over Europe: A first example of the aerosol observing capabilities of Aeolus compared to ground-based lidar, *Geophysical Research Letters*, 48, e2020GL092194, <https://doi.org/10.1029/2020GL092194>, 2021.
- Bohlmann, S., Baars, H., Radenz, M., Engelmann, R., and Macke, A.: Ship-borne aerosol profiling with lidar over the Atlantic Ocean: from pure marine conditions to complex dust–smoke mixtures, *Atmos. Chem. Phys.*, 18, 9661–9679, <https://doi.org/10.5194/acp-18-9661-2018>, 2018.
- Boucher, O., D. Randall, P. Artaxo, C. Bretherton, G. Feingold, P. Forster, V.-M. Kerminen, Y. Kondo, H. Liao, U. Lohmann, P. Rasch, S.K. Satheesh, S. Sherwood, B. Stevens and X.Y. Zhang, 2013: Clouds and Aerosols. In: *Climate Change 2013: The Physical Science Basis. Contribution of Working Group I to the Fifth Assessment Report of the Intergovernmental Panel on Climate Change* [Stocker, T.F., D. Qin, G.-K. Plattner, M. Tignor, S.K. Allen, J. Boschung, A. Nauels, Y. Xia, V. Bex and P.M. Midgley (eds.)]. Cambridge University Press, Cambridge, United Kingdom and New York, NY, USA.

- Dabas, A., Denneulin, M. L., Flamant, P., Loth, C., Garnier, A., and Dolfi-Bouteyre, A.: Correcting winds measured with a Rayleigh Doppler lidar from pressure and temperature effects, *Tellus A*, 60, 206–215, <https://doi.org/10.1111/j.1600-0870.2007.00284.x>, 2008.
- 810 Dai, G., Sun, K., Wang, X., Wu, S., E, X., Liu, Q., and Liu, B.: Dust transport and advection measurement with spaceborne lidars ALADIN and CALIOP and model reanalysis data, *Atmos. Chem. Phys.*, 22, 7975–7993, <https://doi.org/10.5194/acp-22-7975-2022>, 2022.
- de Leeuw, G., Neele, F. P., Hill, M., Smith, M. H., and Vignati, E.: Production of sea spray aerosol in the surf zone, *J. Geophys. Res.*, 105, 29397–29409, <https://doi.org/10.1029/2000JD900549>, 2000.
- 815 Dawson, K. W., Meskhidze, N., Josset, D., and Gassó, S.: Spaceborne observations of the lidar ratio of marine aerosols, *Atmos. Chem. Phys.*, 15, 3241–3255, <https://doi.org/10.5194/acp-15-3241-2015>, 2015.
- Fan, T. and Toon, O. B.: Modeling sea-salt aerosol in a coupled climate and sectional microphysical model: mass, optical depth and number concentration, *Atmos. Chem. Phys.*, 11, 4587–4610, <https://doi.org/10.5194/acp-11-4587-2011>, 2011.
- Flamant, P. H., Cuesta, J., Denneulin, M.-L., Dabas, A., and Huber, D.: ADM-Aeolus retrieval algorithms for aerosol and cloud products, *Tellus A*, 60, 273–286, <https://doi.org/10.1111/j.1600-0870.2007.00287.x>, 2008.
- 820 Flamant, P. H., Lever, V., Martinet, P., Flament, T., Cuesta, J., Dabas, A., Olivier, M., Huber, D., Trapon, D., and Lacour, A.: Aeolus Level-2A Algorithm Theoretical Basis Document, version 5.7, <https://earth.esa.int/eogateway/documents/20142/37627/Aeolus-L2A-Algorithm-Theoretical-Baseline-Document> (last access: 9 November 2022), 2020.
- 825 Flament, T., Trapon, D., Lacour, A., Dabas, A., Ehlers, F., and Huber, D.: Aeolus L2A aerosol optical properties product: standard correct algorithm and Mie correct algorithm, *Atmos. Meas. Tech.*, 14, 7851–7871, <https://doi.org/10.5194/amt-14-7851-2021>, 2021.
- [Floutsis, A. A., Baars, H., Engelmann, R., Althausen, D., Ansmann, A., Bohlmann, S., Heese, B., Hofer, J., Kanitz, T., Haarig, M., Ohneiser, K., Radenz, M., Seifert, P., Skupin, A., Yin, Z., Abdullaev, S. F., Komppula, M., Filioglou, M., Giannakaki, E., Stachlewska, I. S., Janicka, L., Bortoli, D., Marinou, E., Amiridis, V., Gialitaki, A., Mamouri, R.-E., Barja, B., and Wandinger, U.: DeLiAn – a growing collection of depolarization ratio, lidar ratio and Ångström exponent for different aerosol types and mixtures from ground-based lidar observations. *Atmos. Meas. Tech.*, 16, 2353–2379. <https://doi.org/10.5194/amt-16-2353-2023>, 2023.](#)
- 830 ~~[Floutsis, A. A., Baars, H., Engelmann, R., Althausen, D., Ansmann, A., Bohlmann, S., Heese, B., Hofer, J., Kanitz, T., Haarig, M., Ohneiser, K., Radenz, M., Seifert, P., Skupin, A., Yin, Z., Abdullaev, S. F., Komppula, M., Filioglou, M., Giannakaki, E., Stachlewska, I. S., Janicka, L., Bortoli, D., Marinou, E., Amiridis, V., Gialitaki, A., Mamouri, R. E., Barja, B., and Wandinger, U.: DeLiAn – a growing collection of depolarization ratio, lidar ratio and Ångström exponent for different aerosol types and mixtures from ground-based lidar observations, *Atmos. Meas. Tech. Discuss.* \[preprint\], <https://doi.org/10.5194/amt-2022-306>, in review, 2022.](#)~~

- 840 Glantz, P., Nilsson, E. D., and von Hoyningen-Huene, W.: Estimating a relationship between aerosol optical thickness and surface wind speed over the ocean, *Atmos. Res.*, 92, 58-68, <https://doi.org/10.1016/j.atmosres.2008.08.010>, 2009.
- Grandey, B. S., Stier, P., Wagner, T. M., Grainger, R. G., and Hodges, K. I.: The effect of extratropical cyclones on satellite-retrieved aerosol properties over ocean, *Geophys. Res. Lett.*, 38, L13805, <https://doi.org/10.1029/2011GL047703>, 2011.
- Groß, S., Tesche, M., Freudenthaler, V., Toledano, C., Wiegner, M., Ansmann, A., Althausen, D. and Seefeldner, M.:
845 Characterization of Saharan dust, marine aerosols and mixtures of biomass-burning aerosols and dust by means of multi-wavelength depolarization and Raman lidar measurements during SAMUM 2, *Tellus B: Chemical and Physical Meteorology*, 63(4), 706–724, <http://doi.org/10.1111/j.1600-0889.2011.00556.x>, 2011
- Groß, S., Esselborn, M., Weinzierl, B., Wirth, M., Fix, A., and Petzold, A.: Aerosol classification by airborne high spectral resolution lidar observations, *Atmos. Chem. Phys.*, 13, 2487–2505, <https://doi.org/10.5194/acp-13-2487-2013>, 2013.
- 850 Groß, S., Freudenthaler, V., Wirth, M., and Weinzierl, B.: Towards an aerosol classification scheme for future EarthCARE lidar observations and implications for research needs, *Atmos. Sci. Lett.*, 16: 77-82, <https://doi.org/10.1002/asl2.524>, 2015.
- Haarig, M., Ansmann, A., Gasteiger, J., Kandler, K., Althausen, D., Baars, H., Radenz, M., and Farrell, D. A.: Dry versus wet marine particle optical properties: RH dependence of depolarization ratio, backscatter, and extinction from multiwavelength lidar measurements during SALTRACE, *Atmos. Chem. Phys.*, 17, 14199–14217, <https://doi.org/10.5194/acp-17-14199-2017>,
855 2017.
- Haywood, J. M., V. Ramaswamy, and B. J. Soden: Tropospheric aerosol climate forcing in clear-sky satellite observations over the oceans, *Science*, 283, 1299-1303, <https://doi.org/10.1126/science.283.5406.1299>, 1999.
- Hoaglin, D. C., Iglewicz, B., and Tukey, J. W.: Performance of some resistant rules for outlier labelling, *Journal of the American Statistical Association*, 81(396), 991-999, <https://doi.org/10.1080/01621459.1986.10478363>, 1986.
- 860 Huang, H., Thomas, G. E., and Grainger, R. G.: Relationship between wind speed and aerosol optical depth over remote ocean, *Atmos. Chem. Phys.*, 10, 5943-5950, <https://doi.org/10.5194/acp-10-5943-2010>, 2010.
- IPCC, 2021: Summary for Policymakers. In: *Climate Change 2021: The Physical Science Basis. Contribution of Working Group I to the Sixth Assessment Report of the Intergovernmental Panel on Climate Change* [Masson-Delmotte, V., P. Zhai, A. Pirani, S.L. Connors, C. Péan, S. Berger, N. Caud, Y. Chen, L. Goldfarb, M.I. Gomis, M. Huang, K. Leitzell, E. Lonnoy,
865 J.B.R. Matthews, T.K. Maycock, T. Waterfield, O. Yelekçi, R. Yu, and B. Zhou (eds.)]. Cambridge University Press, Cambridge, United Kingdom and New York, NY, USA, 3-32, doi:10.1017/9781009157896.001.
- Jaegle, L., Quinn, P. K., Bates, T., Alexander, B., and Lin, J.-T.: Global distribution of sea salt aerosols: new constraints from in situ and remote sensing observations, *Atmos. Chem. Phys.*, 11, 3137-3157, <https://doi.org/10.5194/acp-11-3137-2011>, 2011.
- Kahn, R. A., Gaitley, B. J., Garay, M. J., Diner, D. J., Eck, T. F., Smirnov, A., and Holben, B. N.: Multiangle Imaging
870 SpectroRadiometer global aerosol product assessment by comparison with the Aerosol Robotic Network, *J. Geophys. Res.*, 115, D23209, <https://doi.org/10.1029/2010JD014601>, 2010.

- Kanitz, T., Lochard, J., Marshall, J., McGoldrick, P., Lecrenier, O., Bravetti, P., Reitebuch, O., Rennie, M., Wernham, D., and Elfving, A.: Aeolus first light: first glimpse, International Conference on Space Optics–ICSO 2018, 111801R, Chania, Greece, 9–12 October 2018, <https://doi.org/10.1117/12.2535982>, 2019.
- 875 Kaufman, Y. J., D. Tanre, and O. Boucher: A satellite view of aerosols in the climate system, *Nature*, 419, 215–223, <https://doi.org/10.1038/nature01091>, 2002.
- Kiliyanpilakkil, V. P. and Meskhidze, N.: Deriving the effect of wind speed on clean marine aerosol optical properties using the A-Train satellites, *Atmos. Chem. Phys.*, 11, 11401–11413, <https://doi.org/10.5194/acp-11-11401-2011>, 2011.
- Kim, M.-H., Omar, A. H., Tackett, J. L., Vaughan, M. A., Winker, D. M., Trepte, C. R., Hu, Y., Liu, Z., Poole, L. R., Pitts, M.
880 C., Kar, J., and Magill, B. E.: The CALIPSO version 4 automated aerosol classification and lidar ratio selection algorithm, *Atmos. Meas. Tech.*, 11, 6107–6135, <https://doi.org/10.5194/amt-11-6107-2018>, 2018.
- Kleidman, R. G., Smirnov, A., Levy, R. C., Mattoo, S., and Tanre, D.: Evaluation and wind speed dependence of MODIS aerosol retrievals over open ocean, *IEEE T. Geosci. Remote*, 50, 429–435, <https://doi.org/10.1109/TGRS.2011.2162073>, 2012.
- Latham, J., and M. H. Smith: Effect on global warming of wind-dependent aerosol generation at the ocean surface, *Nature*,
885 347, 372–373, <https://doi.org/10.1038/347372a0>, 1990.
- Lehahn, Y., Koren, I., Boss, E., Ben-Ami, Y., and Altaratz, O.: Estimating the maritime component of aerosol optical depth and its dependency on surface wind speed using satellite data, *Atmos. Chem. Phys.*, 10, 6711–6720, <https://doi.org/10.5194/acp-10-6711-2010>, 2010.
- Lewis, R. and Schwartz, E.: Sea salt aerosol production: mechanisms, methods, measurements and models – a critical review,
890 American Geophysical Union, <https://doi.org/10.1029/GM152>, 2004.
- Liu, Z., Kar, J., Zeng, S., Tackett, J., Vaughan, M., Avery, M., Pelon, J., Getzewich, B., Lee, K.-P., Magill, B., Omar, A., Lucker, P., Trepte, C., and Winker, D.: Discriminating between clouds and aerosols in the CALIOP version 4.1 data products, *Atmos. Meas. Tech.*, 12, 703–734, <https://doi.org/10.5194/amt-12-703-2019>, 2019.
- Luo, T., Yuan, R., and Wang, Z.: Lidar-based remote sensing of atmospheric boundary layer height over land and ocean,
895 *Atmos. Meas. Tech.*, 7, 173–182, <https://doi.org/10.5194/amt-7-173-2014>, 2014.
- Luo, T., Wang, Z., Zhang, D., and Chen, B.: Marine boundary layer structure as observed by A-train satellites, *Atmos. Chem. Phys.*, 16, 5891–5903, <https://doi.org/10.5194/acp-16-5891-2016>, 2016.
- Madry, W. L., Toon, O. B., and O’Dowd, C. D.: Modeled optical thickness of sea salt aerosol, *J. Geophys. Res.*, 116, D08211, <https://doi.org/10.1029/2010JD014691>, 2011.
- 900 Masonis, S. J., Anderson, T. L., Covert, D. S., Kapustin, V., Clarke, A. D., Howell, S., and Moore, K.: A study of the extinction-to-backscatter ratio of marine aerosol during the Shoreline Environment Aerosol Study, *J. Atmos. Ocean. Tech.*, 20, 1388–1402, [https://doi.org/10.1175/1520-0426\(2003\)020<1388:ASOTER>2.0.CO;2](https://doi.org/10.1175/1520-0426(2003)020<1388:ASOTER>2.0.CO;2), 2003.
- Meskhidze, N. and Nenes, A.: Effects of ocean ecosystem on marine aerosol-cloud interaction, *Adv. Meteorol.*, 2010, 239808, <https://doi.org/10.1155/2010/239808>, 2010.

- 905 Mulcahy, J. P., O'Dowd, C. D., Jennings, S. G., and Ceburnis, D.: Significant enhancement of aerosol optical depth in marine air under wind conditions, *Geophys. Res. Lett.*, 35, L16810, <https://doi.org/10.1029/2008GL034303>, 2008.
- Murphy, D. M., Anderson, J. R., Quinn, P. K., McInnes, L. M., Brechtel, F. J., Kreidenweis, S. M., Middlebrook, A. M., Pósfai, M., Thomson, D. S., and Buseck, P. R.: Influence of sea-salt on aerosol radiative properties in the Southern Ocean marine boundary layer, *Nature*, 392, 62-65, <https://doi.org/10.1038/32138>, 1998.
- 910 O'Dowd, C. D. and de Leeuw, G.: Marine aerosol production: a review of the current knowledge, *Phil. Trans. R. Soc.*, 365, 1753-1774, <https://doi.org/10.1098/rsta.2007.2043>, 2007.
- O'Dowd, C. D., Lowe, J. A., and Smith, M. H.: Coupling sea-salt and sulphate interactions and its impact on cloud droplet concentration predications, *Geophys. Res. Lett.*, 26, 1311-1314, <https://doi.org/10.1029/1999GL900231>, 1999.
- O'Dowd, C. D., Scannell, C., Mulcahy, J., and Jennings, S. G.: Wind speed influences on marine aerosol optical depth, *Adv. Meteorol.*, 2010, 830846, <https://doi.org/10.1155/2010/830846>, 2010.
- Pierce, J. R. and Adams, P. J.: Global evaluation of CCN formation by direct emission of sea salt and growth of ultrafine sea salt, *J. Geophys. Res.*, 111, D06203, <https://doi.org/10.1029/2005JD006186>, 2006.
- Platt, C. M. R. and G. R. Patterson: The interpretation of baseline atmospheric turbidity measurements at Cape Grim, Tasmania, *Journal of Atmospheric Chemistry*, 4, 187-197, <https://doi.org/10.1007/BF00053778>, 1986.
- 920 Prijith, S. S., Aloysius, M., and Mohan, M.: Relationship between wind speed and sea salt aerosol production: A new approach, *Journal of Atmospheric and Solar-Terrestrial Physics*, 108, 34-40, <https://doi.org/10.1016/j.jastp.2013.12.009>, 2014.
- Reitebuch, O.: The spaceborne wind lidar mission ADM-Aeolus, in: *Atmospheric Physics*, edited by: Schumann, U., Springer, 815-827, ISBN 978-3-642-30182-7, https://doi.org/10.1007/978-3-642-30183-4_49, 2012.
- Rennie, M., Tan, D., Andersson, E., Poli, P., Dabas, A., de Kloe, J., Marseille, G., and Stoffelen, A.: Aeolus Level-2B Algorithm Theoretical Basis Document, version 3.40, <https://earth.esa.int/eogateway/documents/20142/37627/Aeolus-L2B-Algorithm-ATBD.pdf> (last access: 7 November 2022), 2020.
- Rennie, M. P., Isaksen, L., Weiler, F., de Kloe, J., Kanitz, T., and Reitebuch, O.: The impact of Aeolus wind retrievals on ECMWF global weather forecasts, *Q. J. Roy. Meteor. Soc.*, 147, 3555–3586, <https://doi.org/10.1002/qj.4142>, 2021.
- Sayer, A. M., Smirnov, A., Hsu, N. C., and Holben, B. N.: A pure marine aerosol model, for use in remote sensing applications, *J. Geophys. Res.*, <https://doi.org/10.1029/2011JD016689>, 2012.
- 930 Shin, D. H., Müller, D., Choi, T., Noh, Y. M., Yoon, Y. J., Lee, K. H., Shin, S. K., Chae, N., Kim, K., and Kim, Y. J.: Influence of wind speed on optical properties of aerosols in the marine boundary layer measured by ship-borne DePolarization Lidar in the coastal area of Korea, *Atmospheric Environment*, 83, 282-290, <https://doi.org/10.1016/j.atmosenv.2013.10.027>, 2014.
- Shinozuka, Y., Clarke, A. D., Howell, S. G., Kapustin, V. N., and Huebert, B. J.: Sea-salt vertical profiles over the Southern and tropical Pacific oceans: Microphysics, optical properties, spatial variability, and variations with wind speed, *J. Geophys. Res.*, 109, D24201, <https://doi.org/10.1029/2004JD004975>, 2004.
- 935 Smirnov, A., Villevalde, Y., O'Neill, N. T., Royer, A., and Tarussov, A.: Aerosol optical depth over the oceans: Analysis in terms of synoptic air mass types, *J. Geophys. Res.*, 100, 16639-16650, <https://doi.org/10.1029/95JD01265>, 1995.

- Smirnov, A., Holben, B. N., Eck, T. F., Dubovik, O., and Slutsker, I.: Effect of wind speed on columnar aerosol optical properties at Midway Island, *J. Geophys. Res.*, 108, 4802, <https://10.1029/2003JD003879>, 2003.
- Smirnov, A., Sayer, A. M., Holben, B. N., Hsu, N. C., Sakerin, S. M., Macke, A., Nelson, N. B., Courcoux, Y., Smyth, T. J., Croot, P., Quinn, P. K., Sciare, J., Gulev, S. K., Piketh, S., Losno, R., Kinne, S., and Radionov, V. F.: Effect of wind speed on aerosol optical depth over remote oceans, based on data from the Maritime Aerosol Network, *Atmos. Meas. Tech.*, 5, 377–388, <https://doi.org/10.5194/amt-5-377-2012>, 2012.
- Stoffelen, A., Pailleux, J., Källén, E., Vaughan, J. M., Isaksen, L., Flamant, P., Wergen, W., Andersson, E., Schyberg, H., and Culoma, A.: The atmospheric dynamics mission for global wind field measurement, *B. Am. Meteorol. Soc.*, 86, 73–88, <https://doi.org/10.1175/BAMS-86-1-73>, 2005.
- Tan, D. G., Andersson, E., Kloe, J. D., Marseille, G.-J., Stoffelen, A., Poli, P., Denneulin, M.-L., Dabas, A., Huber, D., and Reitebuch, O.: The ADM-Aeolus wind retrieval algorithms, *Tellus A*, 60, 191–205, <https://doi.org/10.1111/j.1600-0870.2007.00285.x>, 2008.
- Reitebuch, O.: The Spaceborne Wind Lidar Mission ADM-Aeolus, in: *Atmospheric Physics, Research Topics in Aerospace*, edited by: Schumann, U., ISBN 978-3-642-30182-7, Springer-Verlag Berlin Heidelberg, 815–827, https://doi.org/10.1007/978-3-642-30183-4_49, 2012.
- Trapon, D., Flament, T., Lacour, A. and Stieglitz, H.: L2A user guide, issue V 2.1, <https://earth.esa.int/eogateway/documents/20142/37627/Aeolus-Data-Innovation-Science-Cluster-DISC-Level-2A-user-guide.pdf> (last access: 27 February 2023), 2022.
- Villevalde, Yu. V., Smirnov, A. V., O’Neill, N. T., Smyshlyaev, S. P., and Yakovlev, V. V.: Measurement of aerosol optical depth in the Pacific Ocean and the North Atlantic, *J. Geophys. Res.*, 99, 20983–20988, <https://10.1029/94JD01618>, 1994.
- Wilson, S. R., and Forgan, B. W.: Aerosol optical depth at Cape Grim, Tasmania, 1986–1999, *J. Geophys. Res.*, 107, D8, <https://10.1029/2001JD000398>, 2002.
- Winker, D. M. and Pelon, J.: The CALIPSO mission, *Geoscience and Remote Sensing Symposium, IGARSS ’03, Proceedings, IEEE International*, 2, 1329–1331, <https://10.1109/IGARSS.2003.1294098>, 2003.
- Winker, D. M., Vaughan, M. A., Omar, A., Hu, Y., Powell, K. A., Liu, Z., Hunt, W. H., and Young, S. A.: Overview of the CALIPSO mission and CALIOP data processing algorithms, *J. Atmos. Ocean. Tech.*, 26, 2310–2323, <https://doi.org/10.1175/2009JTECHA1281.1>, 2009.
- Wu, S., Sun, K., Dai, G., Wang, X., Liu, X., Liu, B., Song, X., Reitebuch, O., Li, R., Yin, J., and Wang, X.: Inter-comparison of wind measurements in the atmospheric boundary layer and the lower troposphere with Aeolus and a ground-based coherent Doppler lidar network over China, *Atmos. Meas. Tech.*, 15, 131–148, <https://doi.org/10.5194/amt-15-131-2022>, 2022.
- Zibordi, G., Berthon, J.-F., Melin, F., and D’Alimonte, D.: Cross-site consistent in situ measurements for satellite ocean color applications: The BiOMaP radiometric dataset, *Remote Sens. Env.*, 115, 2104–2115, <https://doi.org/10.1016/j.rse.2011.04.013>, 2011.